NASA TECHNICAL MEMORANDUM NASA TM-75797

THE EFFECT OF PREPARATION CONDITIONS ON THE STRUCTURE AND MECHANICAL PROPERTIES OF REACTION-SINTERED SILICON NITRIDE

Juergen Heinrich

Translation of "Der Einfluss von Herstellungsbedingungen auf das Gefuege und die mechanishchen Eigenschaften von reaktionsgesintertem Siliciumnitrid". Deutsche Forschungs- und Versuchsanstalt fuer Luft- und Raumfahrt, DFVLR, Institut fuer Werkstoff-Forschung, Cologne, Report DFVLR-FB-79-32. 12 September 1979. 102 pages

(NASA-TM-75797) THE EFFECT OF PREPARATION CONDITIONS ON THE STRUCTURE AND MECHANICAL PROPERTIES OF REACTION-SINTERED SILICON NITRIDE (National Aeronautics and Space Administration) 103 p HC A06/MF A01 G3/24

N81-22097

Unclas 22301

NATIONAL AERONAUTICS AND SPACE ADMINISTRATION
WASHINGTON, DC 20546 APRIL 1980

STANDARD TITLE PAGE

1. Report No. NASA TM-75797	2. Government Accession No.	3. Recipient's Catalog No.
4. Title and Subtitle THE EFFECT OF PREPARATION CONDITIONS ON THE STRUCTURE AND MECHANICAL PROPERTIES OF REACTION-SINTERED SILICON NITRIDE		5. Report Date April 1980 6. Performing Organization Code
7. Author(s) Juergen Heinrich		8. Performing Organization Report No. 10. Work Unit No.
9. Performing Organization Name and Address SCITRAN P. O. Box 5456 Santa Barbara, CA 93108		11. Contract or Grant No. NASW-3198 13. Type of Report and Period Covered Translation
12. Sponsoring Agency Name and Address National Aeronautics and Space Administration Washington, D. C. 20546		14. Sponsoring Agency Code

15. Supplementary Notes

Translation of "Der Einfluss von Herstellungsbedingungen auf das Gefuege und die mechanishchen Eigenschaften von reaktionsgesintertem Siliciumnitrid," Deutsche Forschungs- und Versuchsanstalt fuer Luft- und Raumfahrt, DFVLR, Institut fuer Werkstoff-Forschung, Cologne, Report DFVLR-FB-79-32, 12 September 1979. 102 pages

80N 24383

16. Abstract

17. Key Words (Selected by Author(s))	18. Distribution Statement Unclassified - Unlimited		
19. Security Classif. (of this report) Unclassified	20. Security Classif. (of this page) Unclassified	21. No. of Pages 103	22.

NASA-HQ

Summary:

The microstructure of reaction sintered silicon nitride (RSSN) was changed over a wide range by varying the green density, grain size of the silicon starting powder, nitriding conditions, and by introducing artificial pores. The influence of single microstructural parameters on mechanical properties like room temperature strength, creep behavior and resistance to thermal shock has been investigated. The essential factors influencing these properties were found to be total porosity, pore size distribution, and the fractions of α and β Si_3N_4. In view of high-temperature engineering applications of RSSN, potentials for optimizing the material's properties by controlled processing are discussed.

Outline:

1. Introduction

Various recent developments in the fields of energy, raw materials and environmental protection make it seem certain that ceramic high-temperature materials will find increasing use in the future in machine design. Silicon nitride is one of these ceramic high-temperature materials. Its application is being discussed particularly in the production of ceramic motor vehicle gas turbines.

This material exhibits advantages over metals in good creep strength, as well as in resistance to oxidation and corrosive media at high temperatures. But it shows brittle fracture, with its tensile strength and thermal shock resistance too low in comparison with metals.

For this reason, designers of planned high-temperature uses of silicon nitride as a construction material are forced on one hand to seek new ways of designing parts for high dynamic and thermal stresses, and on the other hand, to optimize the mechanical properties through applied materials research and development.

It is the object of this work to investigate the effect of structural parameters on the mechanical properties such as strength, creep and thermal shock behavior of reaction-sintered silicon nitride, and to optimize these properties by directed development of the structure, using variation of the preparation conditions.

2. Literature survey

2.1 Structure of silicon nitride

As early as 1958, Turkdogan et al [1] reported that silicon nitride appears in two different crystallographic forms. Hardie

and Jack [2] showed that both modifications crystallize in the hexagonal system, differing essentially in the fact that the lattice separation in the direction of the crystallographic c axis is about twice as great for α Si_3N_4 and for the β modification. The Si_6N_8 elementary cell of the β phase is derived from the phenacite type (Be_2SiO_4) in which the Be atoms are replaced by Si and the O atoms by N. These findings were confirmed by Ruddlesden and Popper [3] and by Wild et al. [4]. The elementary cell of the βmodification with the layer sequence AB is shown schematically in Figure 1 (projection on the base plane).

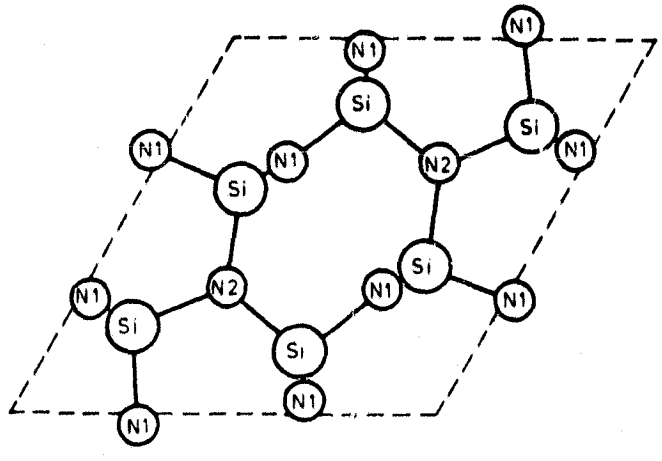

Figure 1. Atomic arrangement in β silicon nitride (according to Wild et al. [4].

Bond lengths (nm)		Distance from the projection plane (units of the c axis)	
$Si-N_1$	0.1730, 0.1739	Si	0.25, 0.75
$Si-N_2$	0.1745	N_1	0.25, 0.75
		N_2	0.25, 0.75

The silicon atoms sit en the centers of irregular N tetrahedra, in which each N atom simultaneously belongs to three tetrahedra. The β structure shows hexagonal channels having a diameter of about 0.15 nm in the direction of the crystallographic c axis. Even large atoms can diffuse easily through these channels. This is later shown to be important in consideration of the reaction kinetics.

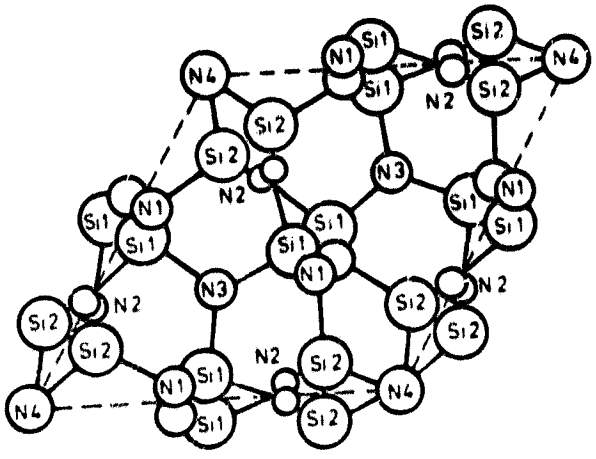

Figure 2. Atomic arrangement in α silicon nitride (according to Wild et al. [4].

Bond lengths (nm)		Distance from the projection plane (units of the c-axis)		
N_1-Si_1	0.1566, 0.1687	Si_1	0.146,	0.646
N_1-Si_2	0.1896	Si_2	0.451,	0.951
N_2-Si_2	0.1893, 0.1562	N_1	0.400,	0.900
N_2-Si_1	0.1795	N_2	0.170,	0.670
N_3-Si_1	0.1781	N_3	0.115,	0.615
N_4-Si_1	0.1782	N_4	0.384,	0.884

Figure 2 shows the $Si_{12}N_{16}$ elementary cell of the α phase projected on the base plane. Here, the layers known from the β structure alternate with their mirror images in the stacking sequence ABCD, giving about twice the lattice distance in the c direction (Table 1). The hexagonal channels in the c direction do not appear any longer, so that diffusion of foreign atoms is more difficult.

While the structure of the β modification is generally assured, there are still contrary views about the α modification. Wild et al. [4] describe α Si_3N_4 as an oxynitride with the total formula $Si_{11.5}N_{15}O_{0.5}$, and this was later confirmed in further investigations [14]. In other works, though, it was shown that

Table 1. LATTICE CONSTANTS FOR THE Si_3N_4 MODIFICATIONS

Modification	α	β
Crystal structure	hex.	hex.
a axis (nm)	0.7748-0.7756	0.759-0.7608
c axis (nm)	0.516 -0.5691	0.2709-0.292
c/a ratio	~ 0.70	~ 0.37
Literature	[2 - 13]	[2 - 10]

much less oxygen, if any, is required for formation of the αmodification [13, 15-18]. It has also been suggested that in the presence of oxygen gas, gaseous SiO forms, and that this reacts with nitrogen, forming α Si_3N_4 and liberating nitrogen [19 - 27].

Although it is not yet certain whether the two Si_3N_4 phases are polymorphic modifications or whether impurities are needed to stabilize them, we can in general say that both modifications occur together in the usual manufacturing process using technical silicon powder, after the nitriding reaction.

2.2 Preparation of silicon nitride

Silicon nitride has no true melting point, but decomposes at 2173 °K [95, 96]. This eliminates the manufacture of formed products via the liquid phase. On the other hand, the predominantly covalent bonding character and the resultant low diffusion rates prevent the sintering processes otherwise common in powder metallurgy [97]. Although attempts have been made to make low-pressure sintering possible by suitable powder preparation and additives [98], the major emphasis in production of formed pieces of Si_3N_4 is on hot-pressing and reaction-sintering. Dense, hot-pressed silicon nitride (HPSN) is produced by compressing silicon nitride powder at temperatures between 1770 and

2070°K and pressures of about 30 MNm^{-2} with addition of sintering aids which form glass phases (e. g., MgO) [99]. For production of porous reaction-sintered silicon nitride (RSSN), in contrast, formed bodies of silicon powder, after shaping, are nitrided to silicon nitride under a nitrogen at about 1673°K [35]. In contrast to HPSN, which loses strength rapidly at temperatures above 1300°K because of the glass phase-forming sintering aids [32], RSSN in many cases actually shows an increase in strength at high temperatures [33, 34].

The injection molding process is suggested for manufacture of RSSN, along with some other processes such as mud casting, isostatic pressing, and web pressing. Because of the variability of the tool shape and the high production rate, this process is particularly suited for mass production of complex parts, and was therefore selected for preparation of the samples to be studied in this work.

2.3 Physical properties of silicon nitride

The physical properties of silicon nitride can in part be deduced from the high proportion of covalent bonding. The low coefficient of thermal expansion, the low density, high hardness and strength, as well as the high decomposition temperature (Table 2) make Si_3N_4 interesting for engineering use.

The wide range for some values such as the E-modulus and the bending strength occur because these data describe both porous reaction-sintered and dense hot-pressed silicon nitride. RSSN can be used up to nearly its decomposition temperature in neutral or reducing atmospheres. It is not resistant to oxidizing atmospheres, though. Nevertheless, this material can be used under oxidizing conditions, as a protective layer of SiO forms on the surface and inhibits oxidation.

Table 2. PHYSICAL PROPERTIES OF Si_3N_4

Crystal structure	hex.	[2]
Decomposition point [°K]	2173	[96]
Theoretical density [g cm^{-3}]		
α modification	3.168-3.188	[3, 4, 9, 10]
β modification	3.19 -3.202	
Thermal expansion coefficient (293 - 1773 °K) [10^{-6} K^{-1}]	3.2	[29]
Thermal conductivity		
(at 473 °K) [10^{-6} m^2sec^{-1}]	4.8	[30]
(at 1673°K) [10^{-6} m^2sec^{-1}]	2.1	[30]
Specific heat [J $g^{-1}K^{-1}$]	0.71	[29]
Electrical resistance [ohm cm]	10^{13}	[97]
Microhardness [Vickers, MN m^{-2}]	16000-18000	[28]
E-modulus		
(at 298°K) [GN m^{-2}]	172-317	[29]
Bending strength		
(at 293°K) [MN m^{-2}]	200 - 1000	[97, 31]

Because of its chemical stability and its high mechanical strength in comparison to other ceramic materials, silicon nitride would be a particularly useful material for use at high temperatures.

2.4 Structure of reaction-sintered silicon nitride (RSSN)

The mechanical properties of RSSN such as bending strength, deformation behavior and resistance to thermal shock are determined essentially by the nature and distribution of the stereometric components of structure and by physical parameters such as the E-modulus and the thermal conductivity. The structural parameters can be varied by the preparation process.

In preparation, of course, several parameters are usually changed at the same time [35, 36]. That leads to difficulties in judging their effects on the mechanical properties [37].

The structure of RSSN is characterized by the proportions of the α and β modifications, their grain sizes, the total porosity, the pore size distribution, unconverted free silicon, and any foreign phases due to the presence of impurities.

In the α phase we distinguish between α needles, which are found on the sample surface and in larger pores, and the very fine-grained so-called "α mat".

The origin of the α needles has been discussed extensively on the basis of TEM photographs. Popper and Ruddlesden [8] showed that the growth of these needles is influenced by impurities in the silicon powder or in the nitriding gas, while Parr and May [38] mention that the presence of oxygen and hydrogen in the nitriding atmosphere is important for the growth of these whiskers. Evans and Sharp [39, 40] describe two whisker types on the form of long thin fibers (with diameters of 0.05 μm) and relatively coarse fibers (with 0.2 μm diameter) having an internal crystalline core surrounded by a thin amorphous layer. This picture was also described by Danforth and Richman [41]. Many of these whiskers show a spherical origin, which often contains impurities such as iron [21]. Jennings et al. [42, 43] concluded from that that these α fibers originate through a VLS (vapor-liquid-solid) mechanism, as Carr and Barlett [44] also suggested. Not all whiskers show this characteristic picture characteristic of the VLS mechanism, and it must be assumed that still other growth mechanisms contribute to formation of the α needles [42, 45], so that we still lack a final explanation.

Several models have been suggested for the mechanism forming the α mat. Thompson and Pratt [46] worked on the basis

that nitrogen has access to the $Si-Si_3N_4$ boundary during the entire nitriding cycle, and that it reacts with Si there. Liberation of new Si surfaces after formation of a Si_3N_4 coating was explained as due to microcracks from the 22% volume increase and the resulting stresses. But microcracks of this nature have not been demonstrated microscopically.

Atkinson et al. [47] suggested a model which does not require microcracks, in spite of the volume expansion and the constancy of dimensions of RSSN material during nitriding (dimensional changes < 0.05% [48]), as the reaction does not occur at the $Si-Si_3N_4$ boundary. After a nitride layer has formed at the surface of the Si particle, silicon diffuses through this layer and reacts with nitrogen in the original pores, so that these are made smaller. As a consequence, empty sites appear in the unreacted silicon grain, and these condense into pores. In these newly formed pores, the nitrogen diffuses in and reacts with Si or SiO in the gas phase. Because of the volume expansion, these newly formed pores become completely refilled with nitride. This model was at first explained with structure photographs, and was confirmed in other works [42]. As the condensation of empty sites into pores was considered improbable, the authors have modified this model in a later work [49]. It was later conjectured that Si_3N_4 nuclei are formed by chemisorption of N_2 onto the Si surface. At these nuclei, nitrogen is transported out of the vicinity of the nuclei by evaporation-condensation or by surface diffusion. At the same time, the nitrogen concentration in the near vicinity of the nuclei (where silicon vaporizes) is too low to be able to form new nuclei. As the nuclear growth advances, a Si_3N_4 coating forms. Pores appear at the places where silicon vaporizes or has diffused away and then they can be refilled as described above.

While the α phase appears preferentially at temperatures below the melting point of silicon, via the gas phase, the

β modification arises from diffusion of N_2 into solid silicon nitride or in the presence of a liquid phase [42, 50, 51]. After a coating has formed, nitrogen can diffuse through the hexagonal channels of the β crystals to the Si-Si_3N_4 boundary and react with Si there. Danforth et al. [52] observed a 'wire-like' growth of β crystals within the silicon grains and explained it as due to occurrence of the hexagonal high-pressure modification of silicon, which forms because of the pressure stresses which occur during nitriding. Metcalfe [53], who criticized this work, showed that the appearance of these 'wires' is an interference phenomenon.

Because of the already-mentioned volume expansion with constant external dimensions, new places must be provided for the reaction product. This new space can be provided through newly appeared porosity, or from the silicon melting together, which would explain the high proportion of the β phase with nitriding temperatures above the melting point of silicon [44]. Formation of the β phase in the presence of a liquid phase is also supported by the observations that impurities in the silicon raw material, which form low-melting eutectics with silicon, promote the occurrence of the β modification [51, 54-56]. The β grains are considerably larger than the α whiskers because of the different mechanism of formation, and the habitus is nearly equiaxial in the mass of grains(41).

The porosity remaining after nitriding can be divided into several groups. One includes the porosity from pore sizes which can be derived from the porosity in the green formed piece, and which has become smaller due to the volume expansion during nitriding. Another group includes new pores formed during nitriding by fusion of Si particles [57] in unconverted silicon at the Si-Si_3N_4 boundary and by formation of the α mat [58]. The latter may be smaller by some orders of magnitude than the former [37].

2.5 Mechanical properties of reaction-sintered silicon nitride (RSSN)

The mechanical properties of RSSN are strongly effected by the development of the structure. We shall first consider the effect of the structure on the strength. In brittle ceramic materials, a crack travels under bending stress from the largest pore or weak site in the surface region of the tensile zone and runs through the sample with little or no plastic deformation. The strength is defined by the stress needed to make the crack advance. In agreement with the theory of Griffith [59] there is a relation between the breaking strength and a critical crack size, according to Equation 1.

(1) $$\sigma_f = 2\sqrt{\frac{E \cdot \gamma}{\pi \cdot a}}$$

σ_f = breaking strength a = failure or crack depth
E = modulus of elasticity
γ = specific surface energy

Thus, the strength depends on the E-modulus, the specific surface energy, and the size of the failure which initiates the crack. The proportion of porosity in a material affects all three values. The specific surface energy is determined by the strength properties of the Si_3N_4 grains or of the grain boundaries, and by the porosity. According to Spriggs [60] the E-modulus shows a dependence on porosity which corresponds with Equation 2.

(2) $$E = E_o \exp(-bP)$$

E_o = E at P = 0
P = porosity
b = constant

The strength can, then, be increased both by reducing the porosity and by reducing the critical crack size.

There are several empirical expressions for the dependence of strength on total porosity [61 - 64]. Thompson and Pratt [46] showed that the relation between porosity and strength of Si_3N_4 can be described with Equations 3 and 4.

(3) $$\sigma = \sigma_o \exp(-bP)$$

(4) $$\sigma = \sigma_o (1-P)^m$$

$\sigma_o = \sigma$ at $P = 0$
P = porosity
b, m = constants

They defined the constant b in Duckworth's Equation (3) [61] as equal to 4.2 for a silicon nitride of high α content, and 6 for a material with high β content. The value for the constant m of the Bal'shin equation (4) was given as 3.4. Rice [65] also determined the dependence of strength on porosity, using strength values determined by several authors, and found good agreement with Equation (3). Jones et al. [66] found a linear relation between strength and density, measured at various degrees of conversion during nitriding. They made the surprising finding that samples having different initial densities have the same strength when they are nitrided to the same density, although the proportion of Si_3N_4 in the sample differs. Rice [65] argued that the reduction in total porosity is the most important quantity increasing the strength. In other works it was also explained that the pore size and the pore size distribution have similar magnitudes of effects on the strength. It could be shown, for instance, that with constant total porosity the strength increases of the pores are made smaller and homogeneously distributed [67-72].

Different judgements have been made about the effect of the proportions of the two modifications, α and β. Although Elias et al. [73] and Jennings et al. [74] always relate low bending strengths to high proportions of the β modification in the material, Mangels and Cassidy [75] found no effect of the α/β ratio on the bending strength. In the literature there are as yet no quantitative data on the grain size distribution in RSSN; that is, effects of grain size on strength have not yet been studied quantitatively. The different opinions about the effects of individual structural parameters on the strength in the literature are due to the fact that there are problems in varying specific single structural parameters. Often the α/β ratio and the pore size distribution are changed simultaneously in different preparation conditions, while both can contribute to the change in strength.

Along with the strength of RSSN, deformation behavior is of particular importance for high-temperature application. For engineering use of RSSN it is interesting that many of the works in the literature on high-temperature creep indicate that the maximal creep elongations are practically always < 1%. It has also been shown that the structural morphology substantially affects the creep bahavior. For instance, Thompson and Pratt [46] and Engel and Thümmler [76] report that under constant experimental conditions at Temperatures above 1200°C in a 4-point bending test, the creep rate and the total elongation increase with increasing porosity. At constant total porosity the creep behavior is also affected by the other structural parameters. Din and Nicholson [77], like Thompson and Pratt [46] showed that the creep strength (high creep strength ≙ low creep elongation) of RSSN increases with increasing proportion of α. Grain boundary sliding and accomodation by grain boundary separation (crack formation) were suggested in [77] and [78] as the creep mechanism. The rise in creep strength with rising α proportion is explained in [77] as due to the fact that in the relatively large β grains there can be displacements, in contrast to the whiskers, and that the displacements make an additional contribution

to deformation. Mangels [71] also described an increase in creep strength in the study of samples with a fine, homogeneous internal structure. Birch and Wilshire [79], who studied creep of Si_3N_4 in a pressure experiment, reported on the contrary that the creep strength diminishes as the initial silicon powder is made finer; this is usually connected with formation of a fine-grained, fine-pored structure during nitriding [37]. In this respect it should be considered that, if, as is often assumed, the creep deformation occurs substantially through the deformation of amorphous grain boundary phases, there should be a rise in creep rate or a reduction in creep strength with diminishing grain size [80]. In none of the works, to be sure, was a quantitative analysis of the grain size distribution performed.

After Glenny and Taylor [81] made the startling observation that RSSN exhibits a considerably higher creep rate at 1000°C than at 1200°C, Gratwohl and Thümmler reported that the atmosphere can have a surprising influence on the creep behavior. For instance, they showed that a material with relatively large creep in air at 1200-1400°C shows substantially lower elongation and creep rate in vacuum at these temperatures. Further studies of this phenomenon led to the observation that the internal oxidation of RSSN contributes to a considerable reduction in creep strength [80, 83, 84]. It is principally the narrow pore channels (finely porous, homogeneous structure) which are responsible for the internal oxidation. The strong drop in creep strength due to internal oxidation can be explained by the formation of an initially amorphous grain boundary phase. The extended primary region, linked with the strong drop in creep rate in the early stages of the experiments is explained as due to reduction of the viscosity by diffusion of impurities to the sample surface and by crystallization of the glass phase. A steady crrep rate is hardly observed at all during the continuing structural change as the experimental period passes. Internal oxidation can be

prevented by the formation of a SiO_2 coating in very finely porous material, which substantially improves the creep strength. This observation, and the observation that strong internal oxidation can occur at low oxidation temperatures because of the very slow formation of the coating [34] might explain the experimental result [81] that a higher creep rate was observed at 1000°C than at 1200°C.

The thermal shock behavior is one of the most important properties for the intended use of RSSN in gas turbine design. Those parameters which affect the thermal shock resistance have been described extensively in, among others, a review article by Shaffer, Hasselman and Chaberski [85] and in works by Hasselman [86, 87]. Here it appears that parameters of particular importance for high thermal shock resistance are not only high values of tensile strength, but also the heat and temperature conductivity, low value of transverse contraction, of the E-modulus, and of the thermal expansion. As some of these parameters depend on the formation of the structure, one must also expect that the thermal shock behavior will depend on the structure, as Coble and Kingery [88], for instance, described for aluminum oxide. In this work, one of the findings was that the thermal shock resistance of Al_2O_3 can be improved by reducing the porosity. The tests done with Si_3N_4 have generally been limited to the comparison of its thermal shock behavior with other materials [89 - 92], from which it can be established that silicon nitride is superior to most ceramic materials because of its small thermal expansion. The few works concerned with structural effects on the thermal shock behavior generally describe only materials with different porosity. In these cases, to some extent, materials with high porosity show better thermal shock resistance than those with low porosity [89, 93], in contrast with the results with Al_2O_3 in [88]. Ziegler [94] studied various commercial grades of RSSN. By means of structural characterization he tried to establish a correlation between

the individual structural parameters and thermal shock behavior. In this work it was mentioned that still other structural parameters than the total porosity, such as macropores and density inhomogeneities in the macro region can affect thermal shock resistance.

3. Experimental

3.1 Sample preparation

3.1.1 Raw material characterization

Four different silicon powders were used as raw materials for preparation of RSSN. In order to investigate the effect of the initial silicon grain size on the structure and the mechanical properties, a silicon powder from the H. C. Starck Company of Berlin and Goslar was used. It was separated by air-sieving into fractions < 10 µm (A), 10 µm - 37 µm (B) and 37 µm - 63 µm (C). For all the other experiments in this work, a silicon powder trademarked "Murex Super Fine" (D) was used. This was provided by the company of Murex Ltd., Rainham, Essex. Figure 3 and Table 3 show the particle size distribution, the specific surface, and the chemical analysis of these powders.

The organic plastic components required for the injection molding process consisted of low-molecular-weight polyethylene waxes and high-molecular-weight polyethylene thermoplastics. Table 4 shows some of the properties of the organic components used which are significant for the injection and burning-out processes.

The dropping point and solidification point must be taken into consideration in selecting the injection temperature (3.1.2), while different burnout temperatures are important for the subsequent burnout process (3.1.3).

Table 3 CHARACTERISTICS OF THE SILICON POWDERS

	A	B	C	D
Particle size (µm)	< 10	10-37	37-63	< 60
Specific surface (BET) (m^2g^{-1})	2,09	0,46	0,24	1,35
d at 50% residue(µm) (Fig. 3)	7	26	51	14
Impurity content (% by weight)				
Fe	0,58	1,01	0,8	0,65
Al	0,17	0,22	0,16	0,23
Ca	0,02	0,014	0,02	0,04
	0,04	0,04	0,05	
C	0,8	0,4	0,4	n. d.
O_2				n. d.

n. d.: not determined

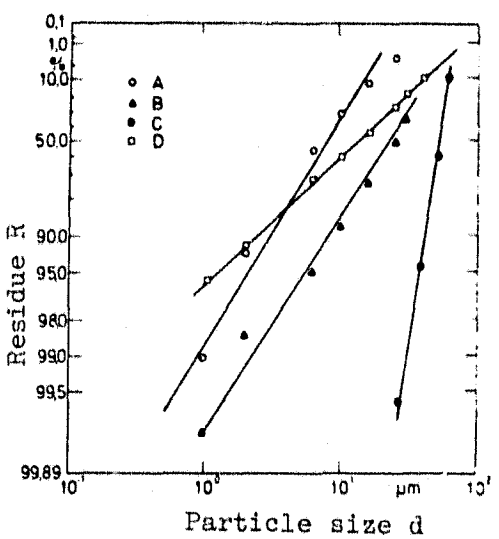

Figure 3. Particle size distribution of the silicon powder.

Table 4. CHARACTERISTICS OF THE ORGANIC COMPONENTS

Component	Dropping Point (°K)	Solidification Point (°K)	Burnout Temp. (°K)	Density at 293°K ($g\ cm^{-3}$)
Thermoplast A (Lupolen x)	408 - 413	405 - 410	583	- 1,0
Wax A (R 21 *)	376 - 381	361 - 366	443	0,93 - 0,95
Wax B (C*)	412 - 417	408 - 413	538	0,99 - 1,01
Wax C (Pa250*)	376 - 380	363 - 367	533	0,91 - 0,92
Wax D (OP*)	373 - 378	347 - 352	483	1,01 - 1,03

x BASF trademark

* Hoechst trademark

3.1.2. Injection molding process

A heatable kneader, type LUK 4 III-2 from the Werner and Pfleiderer company was used to mix and homogenize the organic components with the silicon powder. The liquid plastics were mixed with the silicon powder for about 5 hours at temperatures of about 440°K. The temperature was set above the dropping points of the organic components, and was intended to be limited so that the proportion of organics would not be reduced by excessive evaporation. The granulation needed for the injection-molding process was prepared by cooling with the kneader running. Table 5 shows a typical injection-molding formulation.

A production plastic auger-piston injection-molding machine, the Allrounder 221U/150P of the Arburg company was used for forming (Figure 4). The machine has a maximum injection force of 77 kN. With an auger end diameter of 22 mm there is a maximum specific injection force of 2020 bar.

Table 5. Formula for an injection molding mixture.

Component	Function	% by weight
Silicon powder	matrix	85
Thermoplast A	binder and plasticizer	3
Wax A	lubricant and mold release	3
Wax B	" " " "	3
Wax C	" " " "	3
Wax D	" " " "	3

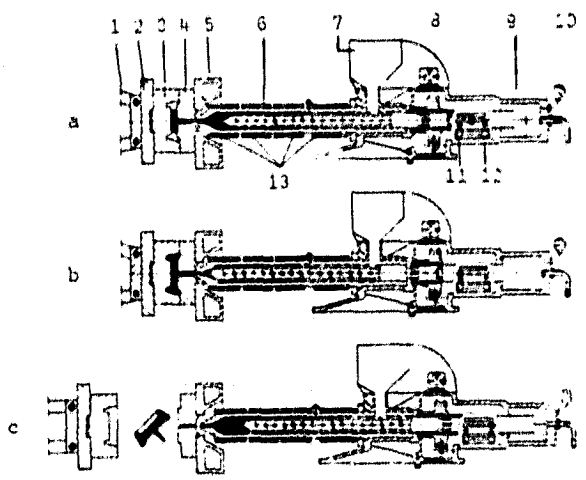

Figure 4. Design and operation of the auger piston injection unit (from [102]).

a. Injection process. b. Standing period with residual pressure. c. Removal of the injection-molded piece.

1. Closure mechanism. 2. Ejector side clamp plate 3. Die 4. Core 5. Injector side clamp plate 6. Plasticizer cylinder 7. Hopper 8. Hydraulic motor. 9. Hydraulic cylinder. 10. Pressure gauge 11. Afterpressure cutoff switch. 12. Auger motion adjustment. 13. Heater.

The granulation fed in from the hopper is plasticized in the heated cylinder and injected into the shaping unit by the auger which acts as the feed and pressurizing element (Figure 4; other information on the injection molding technology in [100 - 107]). The temperature zones in the heatable plasticizer cylinder are determined by the dropping points and the viscosity curve of the organic components used. Depending on the flow behavior of the powder and the content of organic components, they were between 440 and 510°K.

The mold temperature is below the solidification point of the plastic mass, so that the plastic mass solidifies and can be removed from the mold. This temperature should be selected so that the mixture remains fluid until the mold is completely full. Thus, high mold temperatures can prevent inhomogeneities across the sample cross section and feed cone. On the other hand, this temperature must be sufficiently under the solidification point of the lowest-melting organic component in order to prevent bubble formation at the sample surface after removal from the mold. As an appropriate compromise, the mold temperatures were between 310 and 330°K.

Augers having different geometry were used, depending on the flow behavior of the mixture. For high plastic contents and powders with relatively broad particle size distribution (Powder D) a conventional thermoplastic auger with a compression zone and backflow barrier could be used because of the good flow characteristic of the mixture (Figure 5a). At the compression zone in the forward part of the auger the core diamter increases, causing added homogenizing action. The backflow barrier prevents the material from being pressed backward during the injection process (Figure 5a).

When powders with very narrow particle size distribution were used (Powders A, B and C) or at very low plastic contents

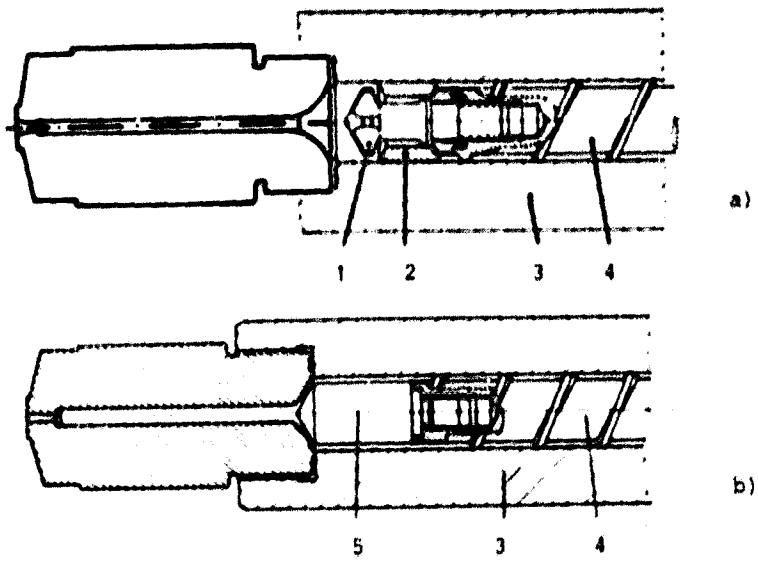

Figure 5a. Auger tip with backflow barrier; cylinder with open nozzle.

Figure 5b. Auger tip without backflow barrier; cylinder with open nozzle.

1. Plasticizer auger. 2. Plasticizer cylinder
3. Backflow barrier. 4. Auger tip

a durometer auger without the compression zone and without the backflow barrier was used (Figure 5b). Because there is a larger space here between the auger core or auger tip and the cylinder wall, even powders which flow poorly can be injected.

When working with mixtures with poor rheological behavior, injection into the mold was also not perpendicular to the separating surface, as shown in Figure 4, but rather it was into the separation plane of the mold, with a vertical arrangement of the plasticizer cylinder. This arrangement makes it unnecessary to have flow diverting channels in the mold, where the masses tend to unmix. The homogeneity of the injected samples can also be improved by optimizing the injection rate and the injection pressure. Table 6 shows schematically the parameters to be optimized for injection molding.

Table 6. PARAMETERS TO BE OPTIMIZED IN INJECTION MOLDING

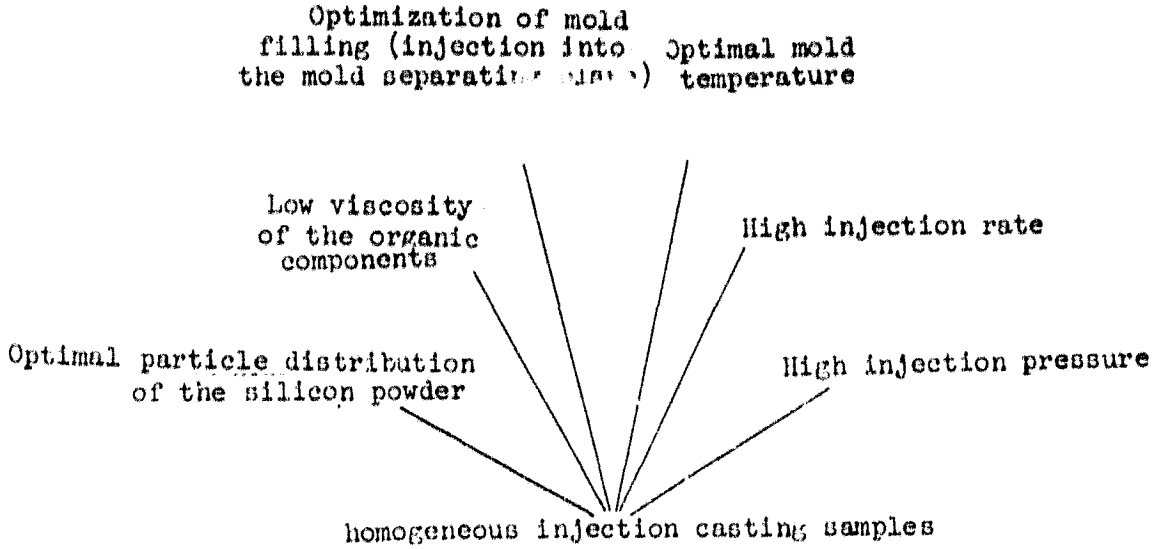

3.1.3. Burning out the organic components

The organic components were burned out in a Heraeus Type KA F 320 fresh-air oven equipped with a five-stage electronic programmer from the Ingenieur-buro Vakuumtechnik company. The temperature was measured and controlled from NiCr-Ni thermocouples placed in the center of the material heated. Flow, diffusion and evaporation processes in the porous sample, similar to those in the drying process of ceramic pieces [105] are responsible for the burning-out process. It is essentially the wall thickness or the sample thickness which determines the burnout time. There is no noticeable shrinkage here with maximum of 20%-by-weight plastics which was used. One may assume that there is a framework of silicon powder with particles in contact, in which the plastic fills the spaces. This is confirmed by the dimensional stability of the samples.

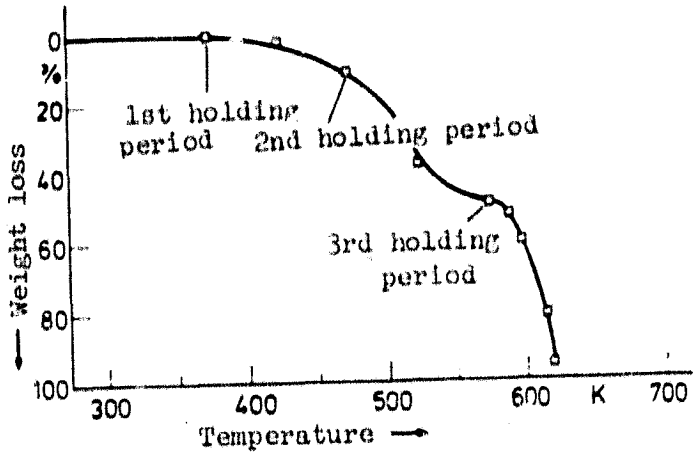

Figure 6. Weight loss on burning out of the organic components of the injection-molded samples, as a function of the temperature.

As the temperature rises during the burning-out process, significant volume changes occur for the organic components, due to the thermal expansion of the binder as well as to the transition of the organic components from the solid state to the liquid and later to the vapor state. Overly-sudden rise in temperature or use of a single organic plasticizer can, therefore, destroy the originally homogeneous structure of the sample because of the too-sudden transition of the organic components from the solid to the liquid or gaseous state [see 108]. For this reason, emphasis was placed on different softening ranges or burnout temperatures when the organic components were selected. (See Table 4.)

The softening range and the weight loss of the injection-molded samples as a function of the temperature were taken into consideration (Figure 6) when the time-temperature program was established. The total burnout times were about 100 hours, with holding periods at 373°K (2 hours), 473°K (10 hours), and 573°K (10 hours) and heating rates from 2.5 to 10 °K/hr with a maximum temperature of 653°K. The maximum temperature

should not be exceeded because the silicon powder is susceptible to oxidation.

3.1.4. Nitriding process

The conversion of the injection-molded and burnt-out samples according to the net formula

(5) $$3Si_{(s)} + 2N_{2(g)} \rightleftharpoons Si_3N_{4(s)}$$

was performed in a vacuum/protective gas oven from the company Ingenieurbüro Vakuumtechnik (Figure 7). This is a double-walled water-cooled all-steel oven with molybdenum heating elements and molybdenum radiation shields.

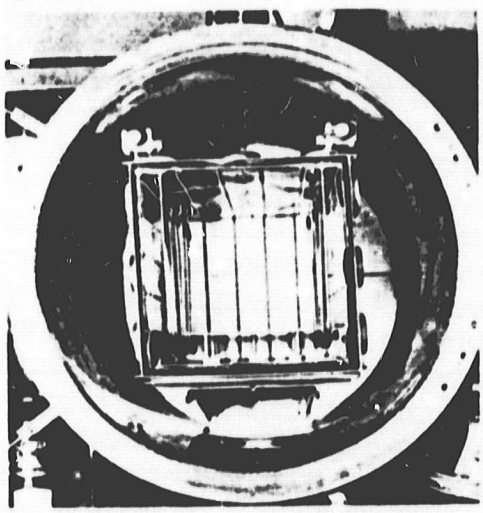

Figure 7. View into the interior of the nitriding oven.

The usable volume of the oven is 175 x 175 x 380 mm. The power supply is designed for a maximum temperature of 1923°K. The temperature is measured and controlled from two W5Re/W26Re thermocouples (7 in Figure 8) placed in the center of the open volume or on the thermal conductors. The temperature is controlled using a PID controller and a five-stage electronic programmer. The latter provides for programming

the heating rates, holding temperatures, and holding times in five steps. The nitriding oven is equipped with a high-vacuum pump system (12-17 in Figure 8) with high-vacuum measurement (9 - 11 in Figure 8). As nitrogen is consumed in the conversion of Si to Si_3N_4, and all the nitriding tests were to be performed under static conditions, i. e., at constant nitrogen pressure, pressure regulation was installed. The MKS Baratron (9 in Figure 8) actuated a magnetic valve (19) through a valve controller (18), so that the nitrogen pressure in the free volume could be held at a constant value. The desired pressure is adjusted at the valve controller.

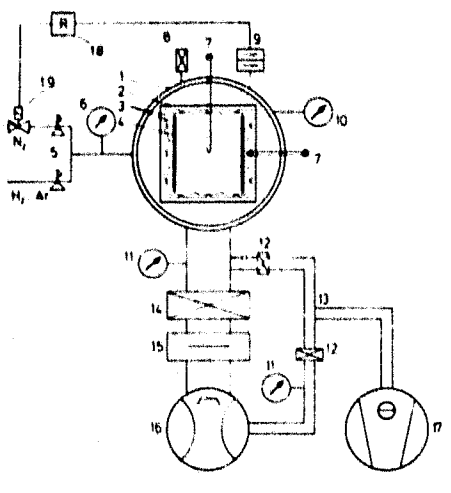

Figure 8. Schematic design of the resistance-heated nitriding oven.

1. Water-cooled stainless steel chamber
2. Water-cooled copper holder
3. Molybdenum radiation shield
4. Molybdenum heat conductors
5. Control valves
6. Spring pressure manometer
7. Temperature measurement point
8. Overpressure valve.
9. MKS Baratron
10. Ionization gauge
11. Thermal conductivity gauge
12. Gate valve
13. Bypass line
14. High vacuum valve
15. Cryo-baffle
16. Diffusion pump
17. Mechanical forepump
18. Valve controller
19. Magnetic valve

Before the actual nitriding process, the samples were outgassed for some hours in high vacuum ($\approx 2 \times 10^{-5}$ mbar) in the nitriding oven at temperatures up to 673°K to remove the last residues of organic components and physically adsorbed gases. Then nitrogen, nitrogen-hydrogen or nitrogen-argon mixtures were added to a pressure which was, according to experience, below the actual experimental pressure because of the expansion of the gases on heating. Because of the exothermic nature of the nitriding reaction and the related danger of overheating the incandescent mass, holding periods were provided from 1453°K and up, and relatively low heating rates of 0.1 °K/minute were selected. The maximum nitriding temperatures were usually 1673°K, i. e., just below the melting point of silicon (T_m Si = 1683°K). The total nitriding time was about 100 hours (Figure 9).

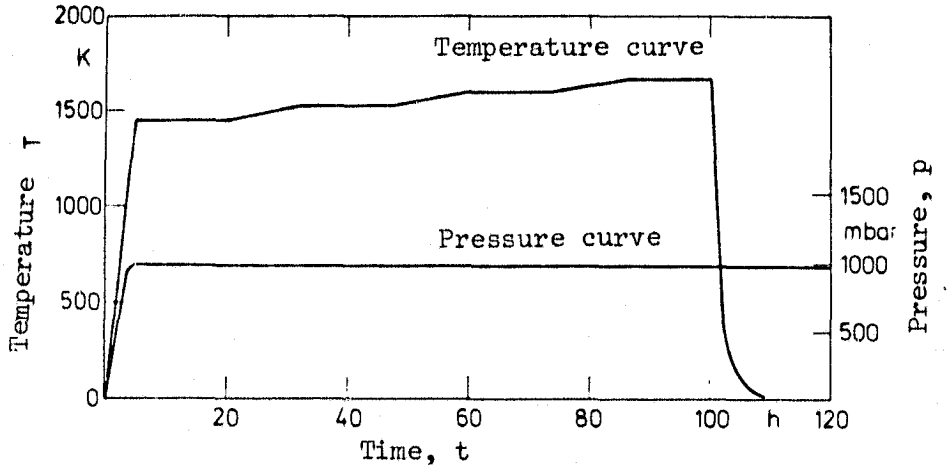

Figure 9. Course of temperature and pressure during a nitriding cycle.

3.2 Quantitative determination of structure

A structure is characterized by those parameters which describe the stereometric structure (grain size, pore size, etc.) and are independent of material-related factors [109]. The

stereometric parameters are characterized by size, shape, volume proportion and distribution with respect to their size and location in the sample. In reaction-sintered silicon nitride, it is principally the proportions of the two modifications, α and β, the grain size and grain size distribution, the total porosity, the pore-size distribution, and non-converted silicon which contribute to differences in the structural morphology [37]. The porous RSSN samples were structurally characterized by determining the degree of reaction and by density measurements using the Archimedean principle. The grain sizes of the α and β modifications were determined on etched or ion-thinned slices using the scanning or transmission electron microscope. The volume proportions of the α and β phases were determined by X-ray. The pore size distribution was determined with an ERBA Science mercury pressure porosimeter and from light-microscopic photographs of sections.

3.2.1 Degree of reaction

The theoretical weight increase on conversion of silicon to silicon nitride by the net formula (5) is 66.49%. The degree of reaction can be determined by determining the weights of the samples before and after the nitriding process:

$$(6)\quad \text{degree of reaction} = \frac{\text{measured weight increase}}{\text{theoretical weight increase}}$$

In this calculation one must take into consideration the proportion of free silicon and that in the Si_3N_4 after nitriding, as well as the proportion of silicon before nitriding and the proportion of evaporated silicon which leaves the pore volumes (other phases could not be detected either by light microscopy or by X-ray).

With:

m_1 = mass of Si before the reaction
m_2 = mass of free Si after the reaction
m_3 = mass of evaporated silicon
m_4 = mass of Si_3N_4 after the reaction

we get:

$$(7) \quad \text{Degree of reaction} = \frac{\Delta\text{weight measured}}{\Delta\text{weight theoretical}} = \frac{m_4 + m_2 - m_1}{1.66\, m_1 - m_1}$$

and with

$$m_4 = 1.66\,(m_1 - m_2 - m_3)$$

it follows that

$$(8) \quad \text{Degree of reaction} = \frac{0.66\, m_1 - 0.66\, m_2 - 1.66\, m_3}{0.66\, m_1}$$

and thence

$$(9) \quad \text{Degree of reaction} = 1 - \frac{0.66\, m_2 + 1.66\, m_3}{0.66\, m_1}$$

Converted into terms of percent by volume, V_v, this gives

$$(10) \quad \text{Degree of reaction} = 1 - [V_v(2) + 2.5\, V_v(3)] < 1$$

Because of the negative correction term in this formula, the degree of reaction is less than 100% in practice. With a measured 90% degree of reaction and 4% free silicon after the reaction (see 4.1.1) the volume proportion of evaporated silicon is 2.4%. If oxides or oxynitrides also occur due to

high oxygen contents in the starting material or in the nitriding gas, those percentages must also be considered in the calculation of degree of reaction.

3.2.2. α and β phase components

The proportions of the α and β phases are determined roentgenographically with a Siemens fine structure goniometer using CuK_α radiation. For these measurements, the RSSN samples were ground to a particle size ≤ 5 µm in a Retsch high-speed micro-mill with a boron carbide holder.

From the goniometer records, the peak heights of the intensities of the β lines (101) and (210) and of the α lines (102) and (210) were evaluated. According to [110], good accuracy is achieved if the ratios of these values are evaluated by the formula:

$$(11) \quad F = \frac{I_{\beta(101)} + I_{\beta(210)}}{I_{\alpha(102)} + I_{\alpha(210)}}$$

and the proportion of the α phase in the total amount of Si_3N_4 is determined from a calibration curve (Figure 10). Values of $\alpha/\alpha + \beta$ from 10% to 90% were found.

3.2.3. Grain size

The grain size in the RSSN was studied on etched sections or on ion-thinned samples in the scanning electron microscope (SEM) and transmission electron microscope (TEM). For the SEM studies the sections were ground and polished as in 3.2.5.2, then etched and vapor-coated with gold. Because of the differing grain sizes of the α and β crystallites it was not possible to make both phases visible with a single etching process. By the time the grain boundaries of the β grains, which are relatively large in comparison to the α whiskers, appeared, the α phase was completely over-etched. Table 7

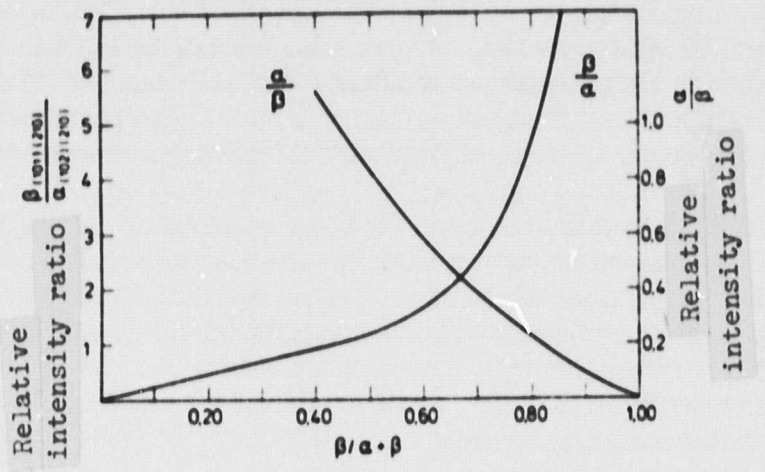

Figure 10. Relative intensity ratios for the lines (101) and (210) of β and of (102) and (210) of α as functions of the proportion of β. [110]

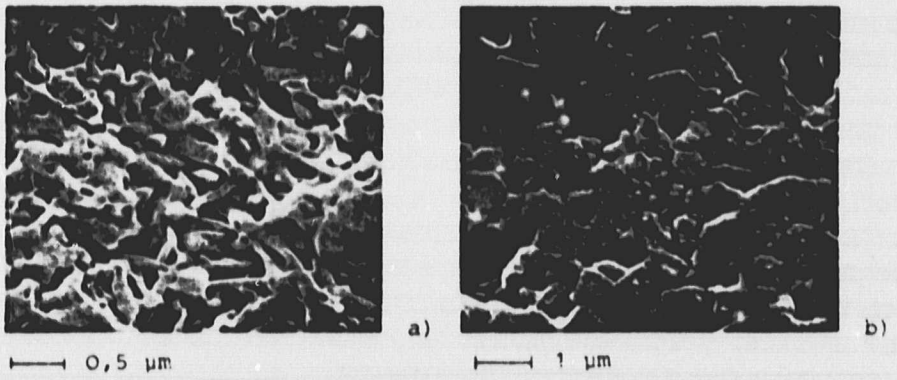

Figure 11. Differing grain sizes and grain morphology of the α and β modifications (SEM, etched sections).

a) α mat
b) β phase

indicates the different etching techniques and their applicability for particle size determination in RSSN.

For this work, the β crystallites were etched chemically (NaOH melt, 673°K, 40 sec.) and the α whiskers were etched by ion bombardment (argon ions, 3 hrs) in an ion thinning apparatus (Figure 11).

Table 7. ETCHING TECHNIQUES FOR GRAIN BOUNDARY ETCHING IN α and β Si_3N_4

Etching method	Etching temperature (°K)	Etching time	α grain boundary etching	β grain boundary etching
Thermal (vacuum)	1473-1673	10 min - 2 hr	too aggressive	satisfactory
Chemical (NaOH melt)	673	40 sec	too	good
Ion bombardment (argon ions)	273	3 hr	good	insufficient

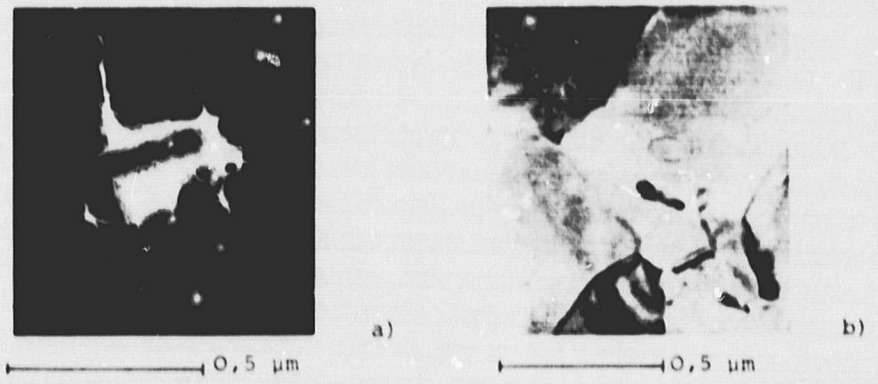

Figure 12. Differing sizes and morphologies of grains of the α and β modifications (TEM, ion-thinned).
a) α whiskers
b) β phase

For investigation in the TEM the samples were first ground to a thickness of about 100 µm on silicon carbide abrasive paper, and then prepared for examination in the ion thinning apparatus. Figure 12 shows TEM pictures of the α and β phases.

3.2.4. Density and total porosity

The density of RSSN was determined using the Archimedean principle by measuring the buoyancy in mercury. The density

is made up of the densities and volume proportions of the separate phases, with the porosity taken into consideration.

(12) $\rho_{\text{measured}} = \sum V_v(\nu) \cdot \rho_\nu$ with $\sum V_v(\nu) = 1$

$V_v(\nu)$ = volume proportions of the phases which occur
ρ_ν = densities of the individual phases.

In the calculation of total porosity, free silicon in particular must be considered along with the Si_3N_4 as solid phases. It follows from (12) that

(13) $$\rho_{\text{measured}} = V_v(Si_3N_4) \cdot \rho_{Si_3N_4} + V_v(Si) \cdot \rho_{Si}$$
$$\text{with } V_v(Si_3N_4) + V_v(Si) + V_v(\text{Pores}) = 1.$$

Then, by eliminating $V_v(Si_3N_4)$ it follows that the volume proportion of porosity is:

(14) $$V_v(\text{Pores}) = 1 - \frac{\rho_{\text{measured}}}{\rho_{Si_3N_4}} - V_v(Si) \cdot \left(1 - \frac{\rho_{Si}}{\rho_{Si_3N_4}}\right).$$

With 5% free silicon, the value for the correction term,

$$V_v(Si) \cdot \left(1 - \frac{\rho_{Si}}{\rho_{Si_3N_4}}\right)$$

is within the measurement accuracy of 1%.

3.2.5 Pore size distributions

3.2.5.1. Mercury pressure porosimetry

The volume proportion of the open porosity and the distribution of open pores having $d \leq 15\ \mu m$ were determined with a mercury pressure porosimeter from the ERBA Science company. Based on the surface tension, σ, of mercury and the contact angle, θ, between Si_3N_4 and Hg, a diameter d for an open cylindrical pore can be assigned

to a hydrostatic pressure, P, according to Equation (15):

(15) $d = -\frac{4}{p}\,\sigma\cos\theta$ with $\sigma = 480\ \mathrm{MN\ m^{-1}}$ and $\theta = 141{,}3\ ^{\circ}$.

For porous ceramic materials in general, to be sure, one must figure on 'bottle pores' (Figure 13). For a mercury pressure of P_1 the volume V_1 of the pore opening with diameter d_1 and the volume V_1' are filled with mercury, until a pore with $d_2 < d_1$ is reached. The same process holds, with pressure increase, for the pore openings with diameters d_2 and d_3. If the pressure is reduced, the pore volumes V_1', V_2' and V_3' remain filled with mercury and hysteresis is observed. With this procedure, then, only the distribution of the 'bottle pores' can be determined, and not the exact distribution of the total open porosity (cf. [111]).

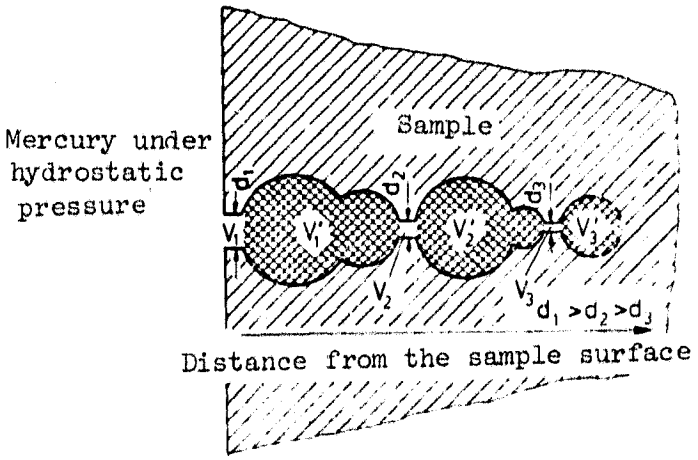

Figure 13. Schematic arrangement of a 'bottle pore'.

The spatial frequency of these pore openings determines the depth of penetration of mercury into the samples. For samples with dimensions 3.5 x 4.5 x 45 mm only a marginal region of the sample was measured at low pressures, corresponding to large pore opening diameters (e. g., d_1 in Figure 13)

because of the limited depth of penetration of the mercury. All the pore openings with the diameter d_1 still present in the rest of the sample volume would only be measured with smaller diameters (higher pressure). These would then be overestimated, and the distribution function which indicates the volume proportion $\Delta V/V_p$ (V_p = total volume penetrated by mercury) per class width Δd as a function of d would be asymmetric (Figure 14).

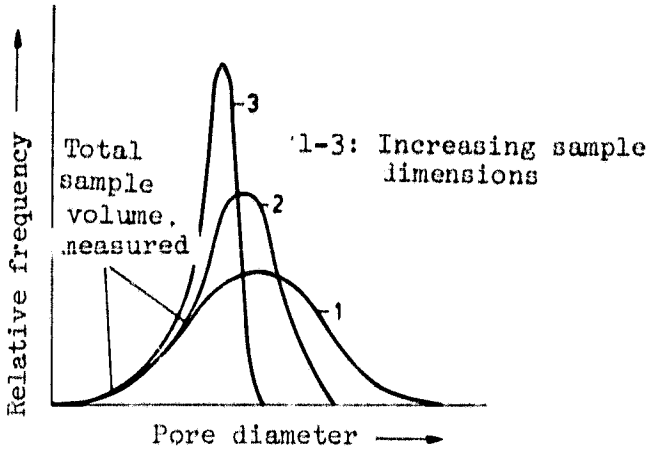

Figure 14. Effect of the sample dimensions on the curve for the pore size distribution function (schematic).

In order to attain realistic distribution functions, it was necessary to grind the samples to a thickness of 1.1 mm. (Further grinding of the sample did not change the distribution function.)

The hysteresis curves, which measure only the volumes of the pore openings, show approximately the same curve as the distribution functions of the thin samples with $h < 1.1$ mm. From this it follows that the ratio V/V' is constant in each Δd interval, so that the curve determined with the mercury porosimeter gives at least an accurate distribution of pore openings. (See Figure 13). The d_{50} values listed in

Section 4 give the diameters which divide the distribution functions into two halves with equal areas. The values for the total open porosity were dependent of the sample dimensions selected here.

In spite of the limited predictive power of this measuring technique, the distribution of the micropores may represent a reasonable parameter for some properties of RSSN, such as the oxidation behavior, as the micropores can affect the formation of the SiO_2 coating which prevents further diffusion of oxygen into the sample.

3.2.5.2. Light microscopic evaluation

For investigation by light microscopy, the RSSN samples were ground on SiC abrasive paper and polished with Al_2O_3 paste. The various phases, Si_3N_4, Si, and pores can be distinguished with the light microscope because of their different reflectivities (Figure 15). The volume proportions of the individual phases can be determined from linear analysis:

$$V_v = L_v/L_o$$

(length L_v in the phase v per measured length L_o).

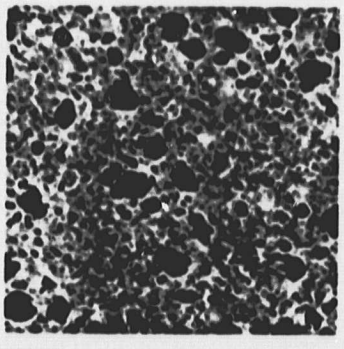

Figure 15. Structure of RSSN (light microscopy, polished section, unetched).

The volume portion of the pores which can be determined in the picture of the section is made up of the contributions of the open and closed pores with $d \geq 1\ \mu m$ and an additive preparation error. At present it is not yet possible to estimate the preparation error, as none of the measuring methods mentioned can determine the ratio of the pores with $d \geq 1\ \mu m$ and $d \leq 1\ \mu m$. We can determine only the sum of the contributions for the open and closed porosity. Evaluation of the pore size distribution of the pores detectable in the light microscope, called macropores in the following, was done with the MOP/AM03 semiautomatic image analysis instrument of the Kontron Company. The percent area of pores in each diameter class was determined at 400 x magnification from a sample area of 0.375 mm^2. The 50% value, d_{50} macropores, which divides the curve into two halves of equal area, was determined from the frequency distribution curve.

3.3 Determination of the mechanical properties

3.3.1. Four-point bending strength

The bending strength was determined on samples with dimensions 3.5 x 4.5 x 45 mm. The samples were tested in the "as fired" state; that is, as they left the nitriding oven. Figure 16 shows schematically the testing system. Because of the great scatter in bending strength due to the brittle breakage of ceramic materials, 25 samples were tested for each experimental point.

(16) $$\sigma_B = \frac{6 \frac{F}{2} \frac{la - li}{2}}{b\ h^2} .$$

3.3.2. Creep behavior

The creep behavior of RSSN with different structural morphology was investigated in the 4-point bending test

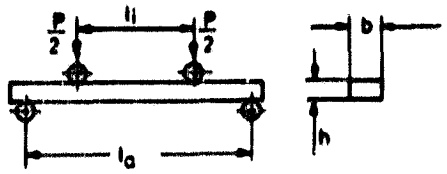

Figure 16. Four-point bending test system (schematic).
li = 20 mm la = 40 mm
b = 4.5 mm h = 3.5 mm

at constant temperature (1573°K) and constant stress (70 Nmm^{-2}) in air. The tests were done with samples of dimensions 3.5 x 4.5 x 45 mm (= h x b x l) with li = 20 mm and e = 10 mm (Figure 17). The samples were ground plane parallel near the supports, but were left with their "as fired" surfaces on the tension side in the area of maximum bending moment (li). The samples were stressed in a resistance-heated oven lined with firebrick, in a clamping arrangement of RSSN. A probe touched the underside of the sample at its center. This probe contained the thermocouple for temperature measurement, and its motion was detected with an inductive motion sensor with a carrier frequency amplifier to indicate the total bending. This type of test has the advantage over the classical tensile creep test that its accuracy is higher for low deformation and flat samples. With very slight elongations, such as occur with RSSN (see 2.2) one cal also avoid the superimposition of bending moments with clamping in the tensile tester. In addition, it is considerably simpler to prepare samples because of the difficulty of processing Si_3N_4. To be sure, a simplifying assumption must be made to calculate the total elongation in the outer tensile fibers of the bending sample.

It is possible to establish a relation with the extension used in the tensile test if we assume that the middle plane of the bending sample, as a 'neutral fiber', experiences no elongation [112]. With the requirement that, as with RSSN, only small bending occurs, we can transfer the relations applicable to the elastic case also to the elastic-plastic case of creep [80]. With this, the error in calculation of plastic elongation according to elasticity theory increases with increasing stress exponents. For small stress exponents of RSSN ($1 \leq n \leq 2$) [80] this error is negligible.

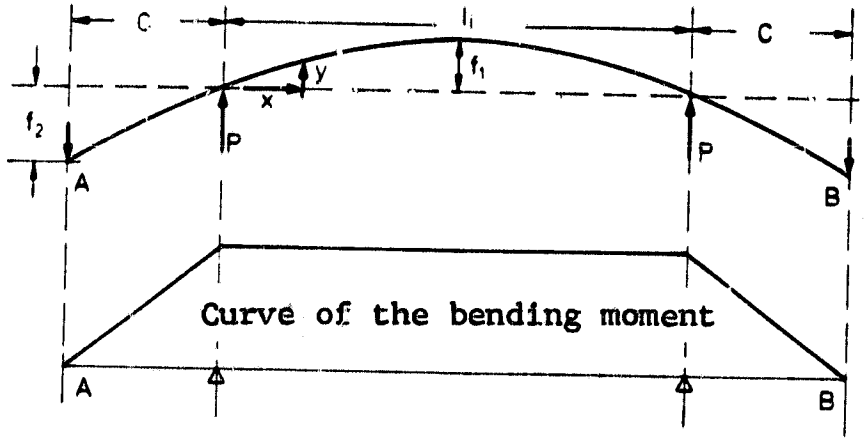

Figure 17. Experimental arrangement and measurements in the 4-point bending test (schematic).

According to [113], then, for samples of rectangular cross-section (Figure 17) stressed in the four-point bending test, we have the relations

$$f_1 = \frac{P}{E\,J}\,\frac{l^2\,c}{8}\,; \qquad f_2 = \frac{P}{E\,J}\,\frac{c^2}{3}\,\left(c + \frac{3\,l}{2}\right). \tag{17}$$

In the creep test, the total bending of the sample, $f = f_1 + f_2$, is measured.

With $E = \frac{\sigma}{\varepsilon}$ and $\sigma = \frac{P\,c}{W}$

the total elongation ε in the outer tensile fiber of the bending sample is found to be

(18) $$\varepsilon = \frac{12\,f\,h}{3\,(1 + 2\,c)^2 - 4\,c^2}\,.$$

3.3.3. Thermal shock behavior

Thermal shock investigations were performed on samples with square cross sections (dimensions: 5 x 5 x 50 mm and 3.4 x 3.4 x 45 mm). The surfaces of the samples were ground with diamond wheels. In order to study the strength behavior after a single temperature change, the samples were held in an induction furnace for 15 minutes at the test temperature, and then thrown into a container of water or oil (T = 298°K). The strength was determined at room temperature before and after this test in the four-point bending test (see 3.3.1). The measure of thermal shock was the so-called critical temperature difference, ΔT_c, at which the thermal stresses developed in quenching exceed the tensile stresses of the material and the strength drops off sharply.

According to [86, 87], unstable crack growth occurs at a critical temperature difference ΔT_c between the temperature of the sample in the oven and the temperature of the quenching medium (Figure 18). This is linked with a discontinuous drop in strength (small crack length in the starting material). Following this rapid drop in strength, there is a region in which the new crack length remains subcritical, so that the strength remains constant. For a temperature difference greater than $\Delta T_c'$ there is a continuous decrease in strength. This is explained by stable crack growth (Figure 18).

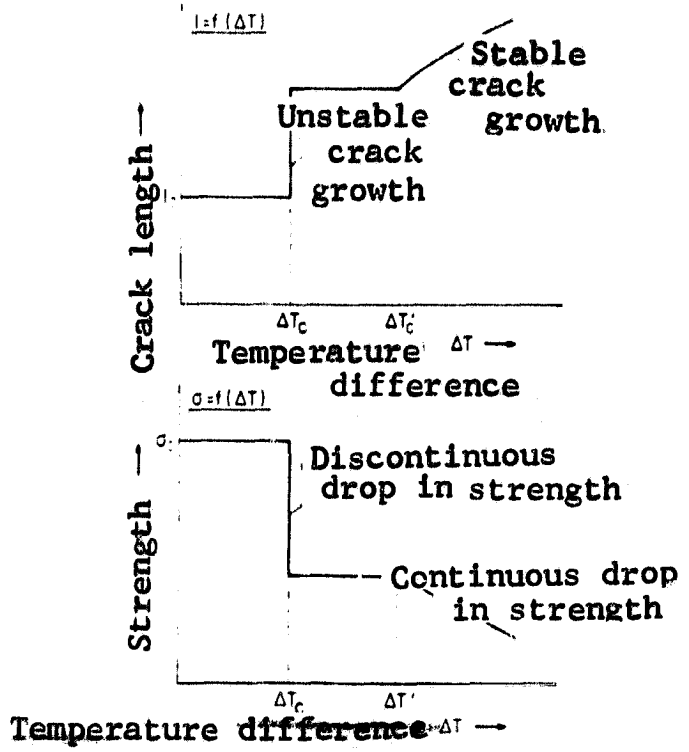

Figure 18. Dependence of the crack length and the strength at room temperature on the temperature difference in quenching (single thermal shock).

Along with the breaking tension, the E-modulus *, the transverse contraction number * and the thermal conductivity of the samples were determined to calculate the thermal shock parameters R and R' (see 4.2.4). The thermal conductivity, λ, was determined from the experimentally measured values of temperature conductivity, a, [127] and literature values of the specific heat (c_p = 700 J/kg °K) and the density, ρ:

(19) $$\lambda = a\, c_p\, \rho$$

The thermal expansion coefficient, α, was taken as $3.3 \cdot 10^{-6}\ K^{-1}$.

---

* I thank Dipl.-Phys. W. Grellner, Erlangen-Nuremberg University, for determining the E-modulus and transverse contraction number.

4. Results and discussion of the relations between preparation conditions, structure and mechanical properties.

4.1 Density and total porosity

The density, or the total porosity, of nitrided samples was varied by varying the proportion of organic components on injection molding. The proportions in the injection moldings used here were between 12.7 and 20% by weight. These yielded green densities (densities in the burned-out state of the samples) of 1.40 to 1.65 g cm^{-3}, and with degrees of reaction above 84%, final densities between 2.23 g cm^{-3} and 2.68 g cm^{-3} ($0.30 \geq V_V(P) \geq 0.15$). The samples were all prepared from powder D with the same nitriding gas composition and constant gas pressure (N_2 : H_2 = 90:10, P = 950 mbar). These nitriding conditions were selected to give optimum room temperature strengths (see 4.5 and 4.6).

As the external dimensions of the samples hardly changed during the nitriding process, the porosity is reduced by the volume increase on formation of Si_3N_4. A green density of 1.91 g cm^{-3} would be needed to produce theoretically dense samples. These green densities are, on one hand, not attainable with the available preparation technology; and on the other hand, with increasing conversion the access of nitrogen to the individual silicon particles is no longer certain. Thus, the reaction is no longer diffusion-controlled, so that complete conversion in acceptable times is no longer possible, especially for samples with thick walls and with use of coarse silicon starting powder. Figure 19 shows, using as an example samples with a green density of 1.57 g cm^{-3}, the decrease in the residual silicon content with increasing degree of reaction. In Figures 19a and 19b one can clearly see the pore formation at the edges of the silicon granules, with the incompletely nitrided

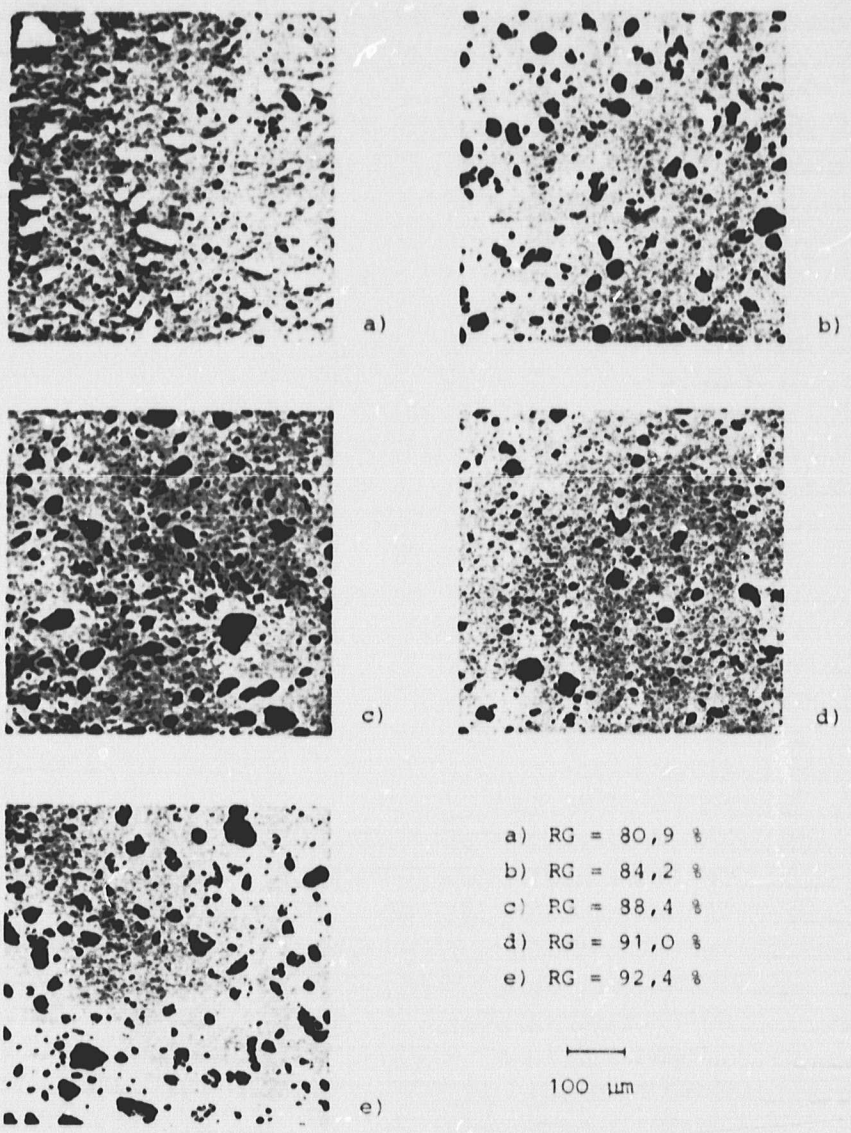

Figure 19. Development of structure in RSSN with increasing degree of reaction (RG) (light microscopy, ground sections, unetched).

gray matrix: Si_3N_4

white phase: unconverted silicon

black phase: pores

samples. This confirms the reaction mechanism suggested by Atkinson, Moulson and Roberts [49] (see 2.3). As the reaction advances, the areas of free silicon become smaller, disappearing completely with complete conversion (Figure 19 c-e).

For samples with a green density of 1.65 g cm^{-3} it was no longer possible to attain a degree of reaction of 70% with the nitriding conditions selected because of the problems mentioned above. In this case the degree of reaction was increased by addition of 1.6% iron by weight to the silicon powder. The degree of reaction rose to 93%. As several authors have reported [114, 115], when iron is added low-melting eutectics form during the nitriding reaction. As is also shown here, they accelerate the reaction and increase the degree of reaction (see also [124])

4.1.1 Bending strength

Table 8 shows the characteristics of the samples, indicating the relation between bending strength and total porosity.

Table 8. RELATION BETWEEN THE DENSITY, OR TOTAL POROSITY, AND THE BENDING STRENGTH

Density ρ ($g\ cm^{-3}$)	Degree of Reaction (%)	Volume proportion of the total porosity $V_V(P)$	Bending strength σ_B ($MN \cdot m^{-2}$)
2,23	95,8	0,30	108 ± 10
2,30	94,3	0,27	144 ± 17
2,42	91,0	0,23	164 ± 14
2,44	84,2	0,20	187 ± 16
2,54	91,0	0,19	203 ± 15
2,53	88,4	0,18	215 ± 10

The total porosity is calculated according to Equation (14) from the density, with consideration of the proportion of free silicon. Here it is assumed that the evaporated silicon amounts to about 2.5% (see calculation of the degree of reaction in 3.2.1.). The dependence of the bending strength on the porosity can be described quite well by means of the empiric relation

(3) $$\sigma = \sigma_o \exp - b\, V_v(P)$$

often applicable to ceramic materials (Figure 20).

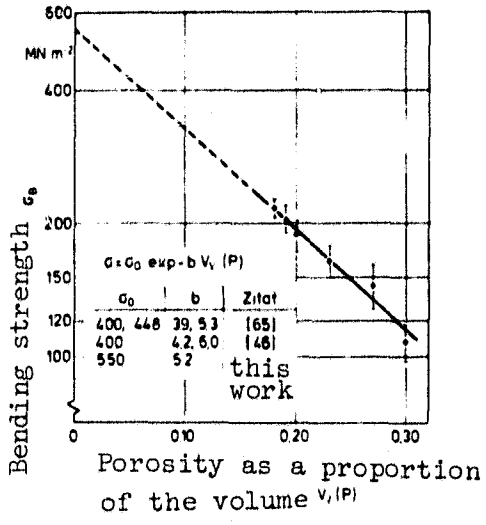

Figure 20. Dependence of the bending strength on the porosity

The constant, b, which is the slope of this line, has a value of 5.2, in rather good agreement with the literature values of 3.9 to 6.0 for silicon nitride [45, 65]. σ_o (σ at $V_v(P) = 0$) is 550 MN m^{-2}. This value is in the range of the usual strength values for dense hot-pressed silicon nitride.

4.1.2. Creep behavior

Figure 21 shows the total elongation as a function of the time in creep tests at constant load and constant temperature for samples with different densities. The total elongation, ε is still less than 2 °/oo for samples with a density of 2.30 g cm^{-3} even after 100 hours. With increasing porosity

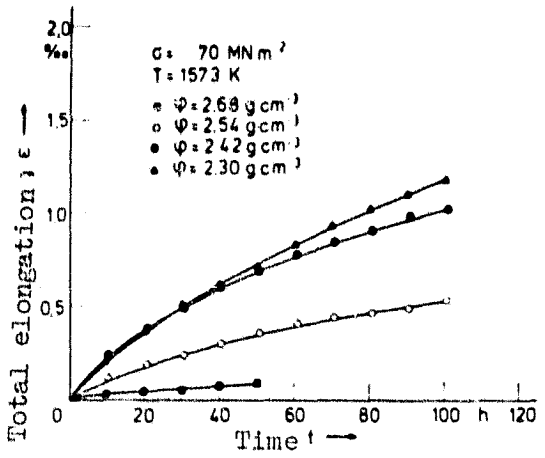

Figure 21. Creep curves of RSSN having different densities, in air at 1573°K and 70 $MN \cdot m^{-2}$.

(decreasing density) the bearing cross-section of the sample is lower, so that the stress is higher for a given load, and the creep rate and total elongation show the expected increase for comparable test periods. Steady creep rate and the tertiary creep region followed by breakage were not observed with these test conditions. If, as described in the literature, the creep mechanism for RSSN is viscous flow of a grain boundary phase with accomodation through grain boundary separation or crack formation, i. e., continuous change in structure during deformation [77, 80], then it is not surprising that a steady creep rate does not appear in practice. Figure 22 shows the creep rate (slope of the curve at ρ = 2.68 g cm^{-3}) at 50 hours, and for the other densities at 80 hours, Figure 21) as a function of the porosity.

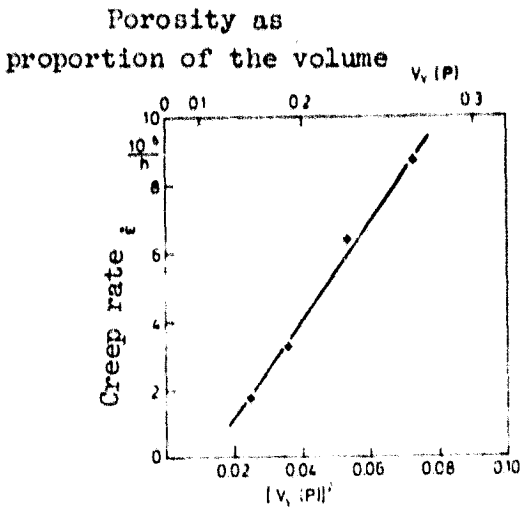

Figure 22. Dependence of the creep rate on the porosity.

It appears from the linear relation between $\dot{\varepsilon}$ and $[V_V(P)]^2$ that in this case the creep rate can be described by the empirical relation

(20) $$\frac{\dot{\varepsilon}_p}{\dot{\varepsilon}_d} = 1 + a \cdot [V_V(P)]^2$$

with $\dot{\varepsilon}_p$ = creep rate of the porous sample
$\dot{\varepsilon}_d$ = creep rate of the dense sample
a = constant

which has already been established for other ceramic materials [116]. If this curve remains linear for even lower porosity, then Figure 22 indicates that for a total porosity of 0.11 there should be no deformation within the measuring period for a stress of 70 MN m^{-2} and a temperature of 1573°K.

It should be noted here that the total porosity alone is not sufficient to describe the dependence of the creep rate and the strength, but that still other structural parameters play their roles.

4.2 Effect of the pore size with constant total porosity

The goal of the investigations performed here was to produce samples with different macropore size distributions but with constant total porosity and with the other structural parameters equal. For this purpose, an organic wax, which could be burned out completely, and which was available as a powder with spherical grains, was sieved into the fractions 0 - 36 µm, 63 - 90 µm, and 125 - 180 µm. Four percent of these fractions, by volume, were mixed into silicon powder D. In contrast with the production of all the other samples used in this work, these powder mixtures were isostatically pressed to a green density of 1.45 g cm^{-3} *. The added wax was burned out before nitriding to produce spherical pores of different sizes.

4.2.1. Structure analysis

Different pore size distributions were determined, due to the different grain sizes of the added waxes (Figure 23). Some of the artificially introduced pores, which can be distinguished from the "natural" pores by their spherical shapes, are marked by arrows in the figure. Table 9 shows the individual structural parameters of these three sample charges.

The value $\bar{d}_{macropores}$ is the mean diameter of the artificially introduced pores. Aside from the macropores, the other structural parameters remained more or less constant, as was expected with the constant preparation conditions.

---

* I thank Rosenthal Technik AG, Plant group IV, Selb, for performing the pressings.

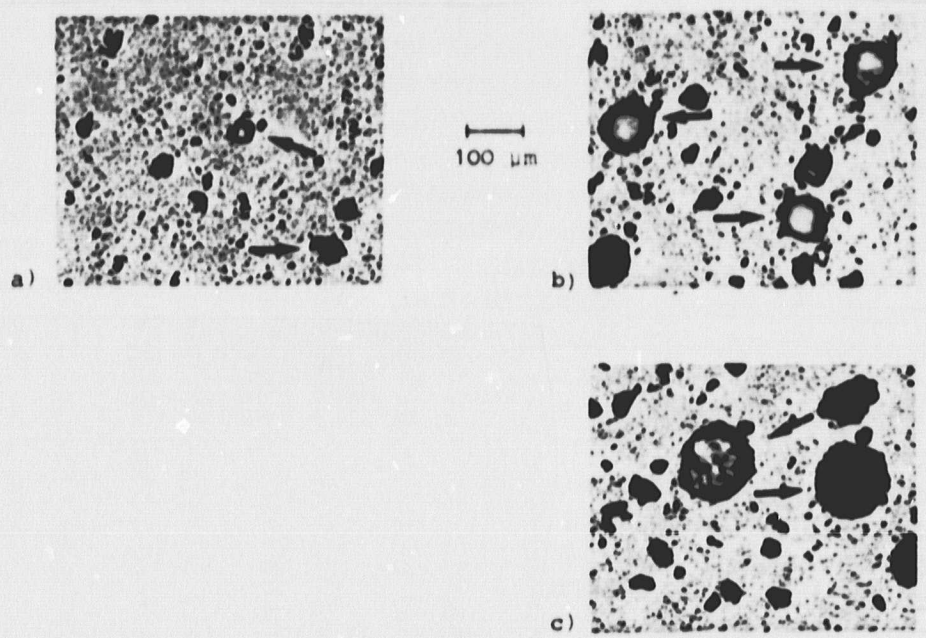

Figure 23. Artificial pores produced with waxes which could be burned out. Some, which can be distinguished from the natural pores because of their spherical shape, are indicated by arrows. (light microscopy, ground sections, unetched).

Wax particle size: a) 0 - 36 µm
b) 63 - 90 µm
c) 125 - 180 µm

Table 9. STRUCTURAL PARAMETERS OF THE RSSN SAMPLES WITH ARTIFICIAL PORES

Wax particle size (µm)	σ ($g \cdot cm^{-3}$)	Degree of reaction (%)	$\alpha/\alpha+\beta$	d_{50} micro-pores ($\mu m \cdot lo^{-1}$)	$\bar{d}$ macro-pores (µm)	σ_B ($MN \cdot m^{-2}$)
0 - 36	2,39	92,8	0,71	1,37	48	140 ± 12
63 - 90	2,39	92,5	0,73	1,29	66	119 ± 18
125 - 180	2,41	90,1	0,64	0,97	100	101 ± 14

4.2.2. Bending strength

The bending strength is plotted in Figure 24 as a function of the mean pore size of the artificially introduced pores. The natural pores, which are smaller than the newly introduced ones, are not considered, as a crack usually propagates from the largest pores in the surface region of the tensile zone.

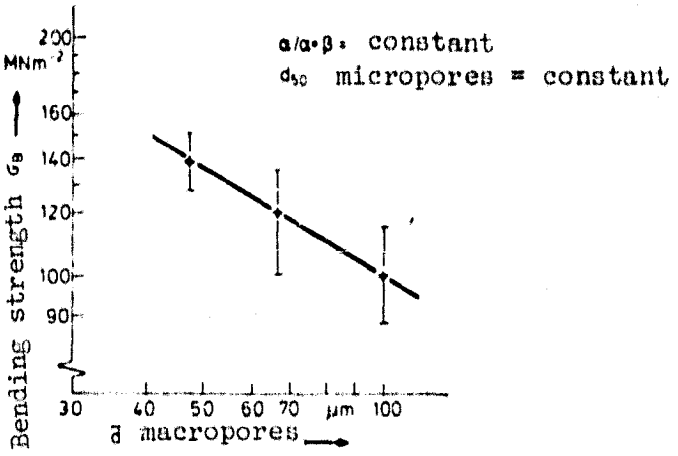

Figure 24. Effect of macropores on bending strength.

If we consider a pore as a sharply defined crack, then the breakage can be described using Griffith's relation (1). The relation between the size of a fault a and the strength, σ_B, can be derived either from the specific rupture surface energy γ or from the crack ductility K_{Ic}. There is a relation between the two quantities:

(21) $$K_{Ic} = \sqrt{2 \gamma E}.$$

The relation between σ_B, a and γ or K_{Ic} is:

(22) $$\sigma_B = \frac{K_{Ic}}{\sqrt{a}\, Y} = \sqrt{\frac{2 \gamma E}{a}}\, \frac{1}{Y}.$$

The value Y depends on the nature of the fault. (Evans and

Tappin [117] have extensively discussed the problems in the fracture mechanistic consideration of pores.) If one considers a pore as a semicircular surface crack, then $Y = 1.16$ [125].

If the strength is plotted versus the fault size, a, on log-log paper, this must according to Equation (1) give a straight line with a slope of $-\frac{1}{2}$. In Figure 24 there is a slope of -0.47, and thus good agreement with the predicted value. Calculation of K_{Ic} according to Equation (22) gives values of 1.13 MN $m^{-3/2}$, 1.12 MN $m^{-3/2}$, and 1.17 MN $m^{-3/2}$ for the three different pore sizes. Direct measurements of K_{Ic} on the same materials gave a value of $\sim$ 1.53 MN $m^{-3/2}$ for all three materials [118]. The fact that the calculated value of K_{Ic} based on the mean pore size is too low is understandable because the break propagates from the largest pore, not from an average one. For a more accurate consideration it would be necessary to determine the fracture-initiating pore for each sample, and even pores below the surface would have to be considered.

4.2.3. Creep behavior

Figure 25 shows the curve for total elongation versus time at 1573 °K and 70 MN m^{-2} for the samples with different macropore sizes. Although the mean macropore size changes by more than 100%, the creep curves are almost identical, and the sample with the largest macropores actually shows the least deformation. As the proportion of artificial macropores is less than 4% of the sample volumes (see 4.2) and the pore size distribution of the natural macropores and micropores has hardly changed (Table 9), these samples show very similar oxidation behavior. (The proportion of open porosity was about 23% for all three series.) On heating to incandescence in air at 1573°K the samples with $\bar{d}_{macropores}$ equal to 48 µm and 66 µm showed the same weight increase. The weight increase was slightly lower for the samples with

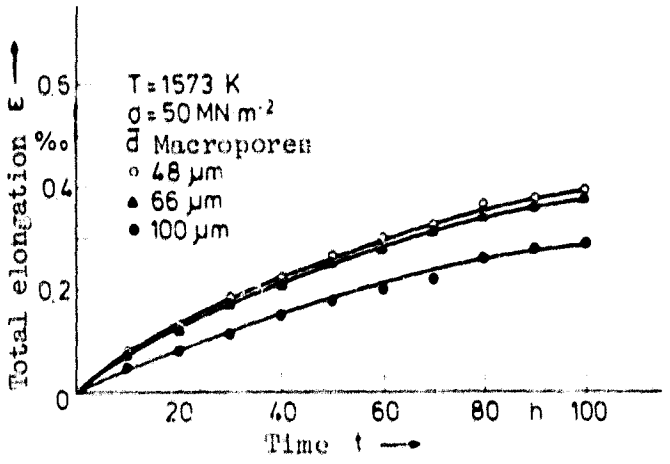

Figure 25. Creep behavior of RSSN with different macropore sizes in air at 1573°K and 70 MN m^{-2}.

$\bar{d}_{macropores}$ = 100 µm. As is shown more extensively later (see 4.3.2 and 4.4.4), the micropores are responsible for the oxidation behavior of RSSN. With small micropore diameters a protective SiO_2 layer forms relatively quickly at the sample surface, strongly inhibiting further oxidation. With larger micropores, on the other hand, there is increased internal oxidation of the samples. As is shown quite extensively in [80], this internal oxidation leads to formation of amorphous oxide phases, so that the Si_3N_4 grains can slide past one another due to the viscous flow of amorphous grain boundary phases. That is why these samples show very similar creep behavior in spite of the very different pore sizes of the artificial macropores.

4.2.4 Thermal shock behavior

Figure 26 shows the dependence of the bending strength on the quenching temperature difference for quenching in water and oil (sample dimensions: 5 x 5 x 50 mm). Up to 1400 °K no strength drop is observed with oil quenching;

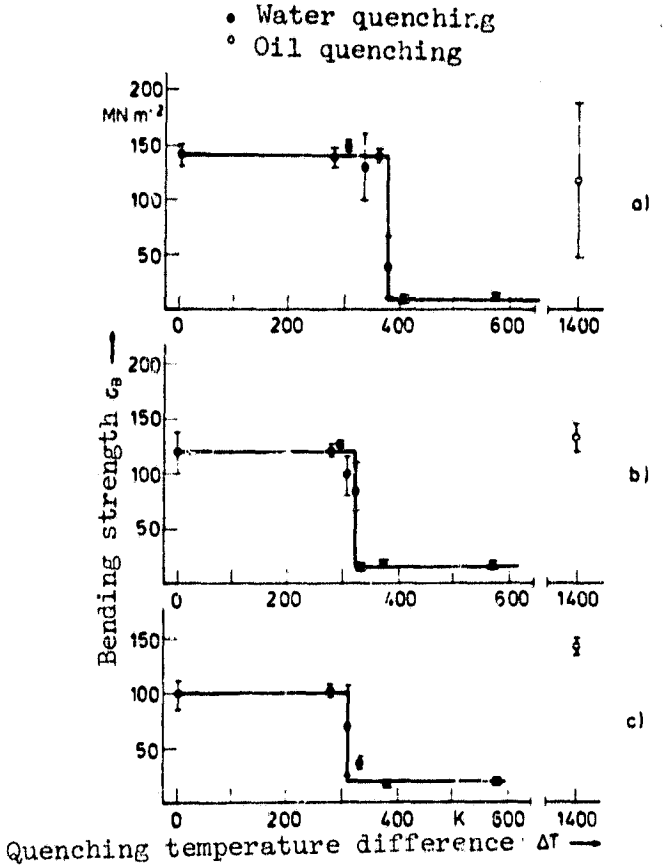

Figure 26. Bending strength as a function of the quenching temperature difference for samples with different macropore sizes (single thermal shock, quenching medium oil or water).

Size of the macropores:

a) 48 µm
b) 66 µm
c) 100 µm.

that is, the critical temperature difference for crack initiation, ΔT_c (see 3.3.3) is greater than 1400°K for these sample dimensions and quenching conditions.

Because of the higher heat transport number on quenching in water, the temperature gradient in the sample is higher, so that the thermal stresses induced are greater than with quenching in oil, and as a result the critical temperature difference is moved to lower values.

With water quenching, the critical temperature difference is between 300 and 375°K, and ΔT_c decreases with increasing porosity (Figure 26; Table 10). This result agrees with the studies of Hasselman [87], who explained the drop of ΔT_c as due to increasing critical crack size (pore size). The strength also decreases with increasing pore size (see 4.2.2), although the E modulus and, therefore, the transverse contraction number remain constant (Table 10).

The experimental results can be explained well with the parameters defined by Hasselman [86], which serve as measures for the resistance to thermal shock stress:

(23) $$R = \frac{\sigma(1-\nu)}{\alpha \cdot E}$$

and

(24) $$R' = \frac{\sigma(1-\nu)}{\alpha \cdot E} \cdot \lambda = R \cdot \lambda ,$$

with σ = bending strength
ν = transverse contraction number
α = coefficient of thermal expansion
E = modulus of elasticity
λ = thermal conductivity.

From the relative values of R' and ΔT_c one can recognize the good agreement between the calculated and experimental values (Table 10). The calculated values of R and R' confirm the experimental finding of a decrease in ΔT_c with increasing pore size.

Table 10. PHYSICAL PROPERTIES, THERMAL SHOCK PARAMETERS AND CRITICAL TEMPERATURE DIFFERENCE OF SAMPLES WITH DIFFERENT MACROPORE SIZES.

Wax particle size (μm)	E ($GN \cdot m^{-2}$)	$1-\nu$	a ($cm^2 sec^{-1}$)	λ ($Wm^{-1}K^{-1}$)
0 - 36	161	0,78	0,1	16,6
63 - 90	167	0,77	0,097	16,1
125 - 180	165	0,76	0,1	16,6

Wax particle size (μm)	R (°K)	R' (Wm^{-1})	ΔT_c (°K)	Relative Values R'	Relative Values ΔT_c
0 - 36	206	3410	375	1	1
63 - 90	166	2680	313	0,79	0,83
125 - 180	141	2340	300	0,69	0,8

4.3 Effect of the proportions of the α and β phases

The contradictory statements in the literature on the effect of the α/β ratio on the mechanical properties of RSSN stimulated the following investigations. They began with establishing that the α/β ratio could indeedbe changed considerably by varying the preparation conditions, although other structural parameters, such as the pore size distribution of the macropores, change at the same time (see 4.4 - 4.6). Thus, evaluations of the effect of the α/β ratio are no longer possible. If in these cases one considers only the relation between the proportion of α and the strength, one finds both a rise and fall of the strength, as well as constancy, with rising α content. Therefore, we attempted to vary the α proportion in such a manner that the macropore size distribution should remain constant.

Table 11. STRUCTURAL PARAMETERS AFTER HEATING TO INCANDESCENCE.

T_{max} (°K)	t (hr)	ρ ($g \cdot cm^{-3}$)	$\alpha/\alpha+\beta$	d_{50} micropores ($\mu m \cdot 10^{-1}$)	d_{50} macropores (μm)
1753	10	2,53	0,78	0,64	30
1753	20	2,53	0,78	0,84	31
1753	40	2,54	0,76	1,02	31
1753	80	2,54	0,75	1,00	32
1873	8	2,51	0,56	1,40	28
1873	16	2,54	0,50	1,60	29
1973	16	2,47	0,16	1,70	30

For this purpose, a sample charge was nitrided at a gas pressure of 270 mbar, a nitrogen/hydrogen ratio of 90/10 and a maximum temperature of 1673°K. This established a value for $\alpha/\alpha + \beta$ Of 0.80 at a density of 2.46 g cm^{-3} (degree of reaction = 84.6%). These samples, which served as the starting material, were heated for 8 - 80 hours at temperatures between 1753 and 1973°K at a nitrogen/hydrogen ratio of 90/10 and a gas pressure of 950 mbar. Table 11 shows the change in individual structural parameters.

By means of the heating above the melting point of silicon (1683°K) the proportion of free silicon was reduced through further reaction with nitrogen, and as a result the densities of the samples increased slightly in comparison with the starting material. At 1973°K and a heating period of 16 hrs the Si_3N_4 began to vaporize, as is noticed in the slight decrease in density. Heat treatments at 1753°K and holding periods up to 80 hours had practically no effect on the α/β ratio. A change in the proportion of α could be observed only above a temperature of 1873°K.

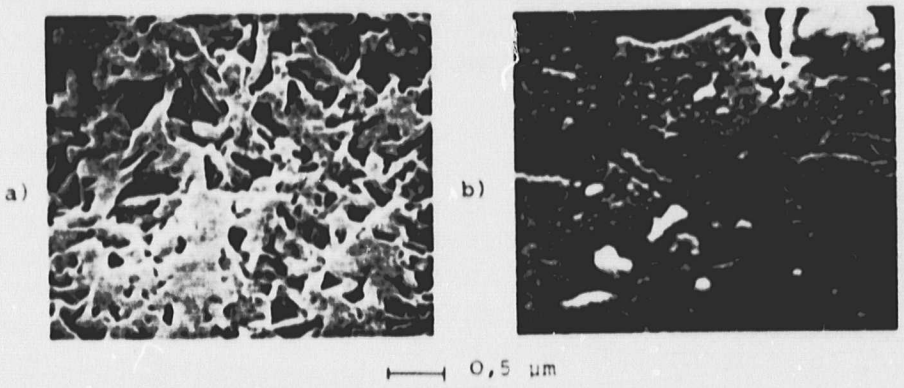

Figure 27. Differing grain sizes and grain morphology of the α and β modifications (scanning electron micrographs, ground sections, etched).
a) α phase b) β phase

Figure 27 shows the difference in grain sizes between the α mat and the relatively densely packed β grains. (More on the grain sizes of the α and β modifications and their developmental histories in 2.3 and 4.4.2.) The pores visible within the α mat agree in order of magnitude with the micropore diameters measured with the pressure porosimeter (Table 11). The micropore diameter rises with increasing α content, while the macropores do not change significantly in size. As it has not yet been possible to visualize both the α and the β grains with a single measuring method, quantitative grain size analysis was not possible.

4.3.1. Bending strength

With diminishing α content; that is, (under these experimental conditions) with increasing micropore diameters, the strength decreases for constant macropore diameter (Figure 28). This indicates that still other structural characteristics than the macropores affect the strength. As the value of K_{Ic} measured for these samples rises with diminishing α content

($\alpha/\alpha+\beta$ = 0.76, K_{Ic} = 1.67 MN $m^{-3/2}$; $\alpha/\alpha+\beta$ = 0.16, K_{Ic} = 2.23 MN $m^{-3/2}$). it is not immediately possible to explain this result. It would be necessary to consider also the effect of grain growth and the potential alteration in the shape of the micropores and macropores during the heat treatment, so that explanation of this result would become very complex.

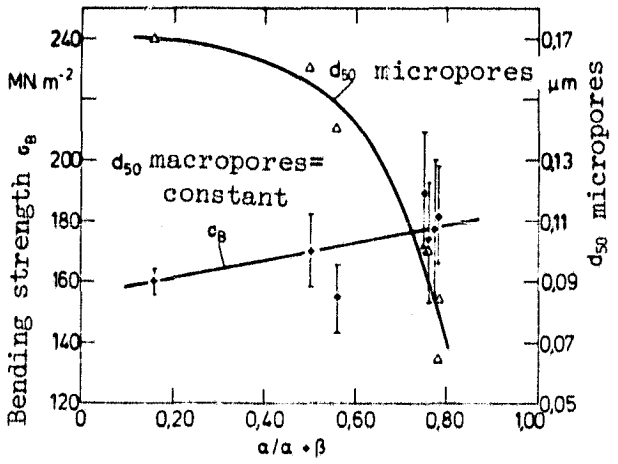

Figure 28. Effect of micropores and the α/β ratio on the bending strength (d_{50} macropores $\approx$ 30 μm).

It should be mentioned, though, that individual structural parameters may change oppositely due to different preparation conditions (e. g., high α proportion with high micropore diameter, and conversely). Thus, if the bending strength is plotted versus the proportion of α without consideration of the other structural parameters, an opposing tendency is observed because under some circumstances the effect of other quantities predominates.

4.3.2. Creep behavior.

Figure 29 shows a plot of total elongation versus the time at 1573°K and 70 MN m^{-2} for materials with high α content and with high β content ($\alpha/\alpha+\beta$ = 0.76 and 0.16, respectively; see Table 11). The material with high β content exhibits a higher creep rate or higher total elongation at comparable times. But, as Table 11 shows, this material also has almost double the micropore diameter, d_{50} micropores. As previously mentioned in 4.2.3, the micropore size is responsible for the oxidation behavior of RSSN. On heating at 1573°K in air, a higher weight increase can be seen with rising micropore diameter (rising β content), due to increased internal oxidation of the samples, although the high-β samples, at 5%, show a far lower proportion of open porosity than the high-α samples at 20% (Figure 30).

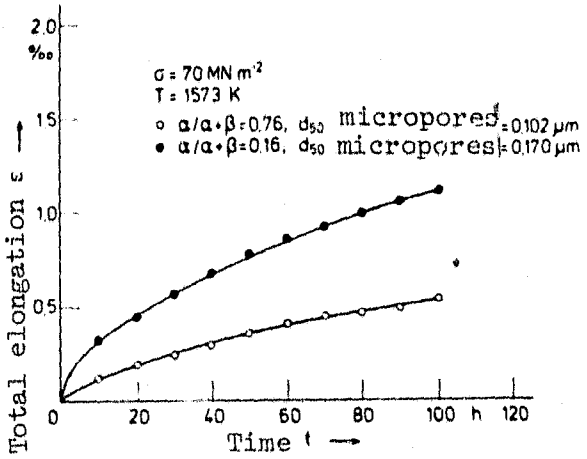

Figure 29. Creep curves of RSSN with different proportions of α in air at 1573°K and 70 MN m^{-2}.

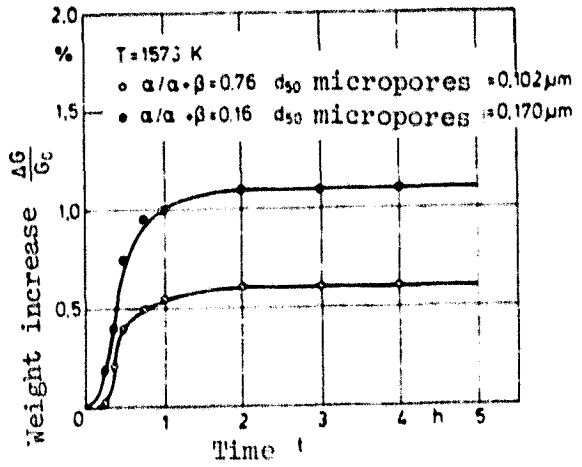

Figure 30. Oxidation curves for RSSN with different proportions of α at 1573°K in air.

Because of this poorer oxidation behavior (formation of amorphous grain boundary phases; sliding of the Si_3N_4 grains due to viscous flow of these amorphous grain boundary phases [80], see 4.2.3) the material with high β content shows a higher creep rate in spite of the fact that the β crystals are relatively large in comparison with the α whiskers (high α content: $\dot{\varepsilon}$ at 80 hours = $3.8 \cdot 10^{-6}$ hr^{-1}; high β content: $\dot{\varepsilon}$ at 80 hours = $10 \cdot 10^{-6}$ hr^{-1}).

4.4 Effect of the initial silicon particle size

In order to investigate the effect of the initial silicon particle size on the structural development and on the mechanical properties, the starting powders A, B, and C were injection-molded to give samples with green densities of 1.40 g cm^{-3} and 1.50 g cm^{-3} by varying the proportion of the organic constituents. These samples were nitrided for 100 hours at a gas pressure of 950 mbar in a mixture of 90% N_2 and 10% H_2 by volume (see 4.5). This gave final densities of ~ 2.2 and ~ 2.4 g cm^{-3}, respectively. (Table 12).

4.4.1 Course of the reaction

Figure 31 shows the time-temperature program and the course of the reaction during nitriding, using samples with a green density of 1.40 g cm^{-3} for examples. (Samples with the green density of 1.5 g cm^{-3} show the same course, except that the degree of reaction at the end of the reaction is somewhat lower; see Table 12). The course of reaction during the period was calculated from the consumption of nitrogen during nitriding. The total nitrogen consumption corresponded to the degree of reaction which had been calculated from the weight increase after the complete nitriding cycle corresponding to Equation (6). With decreasing initial silicon particle size, the degree of reaction increased at relatively low nitriding temperatures. It follows from that, that when finer starting powders are used the total reaction time for complete conversion is considerably reduced and the final temperature can be reduced (Figure 31). The degree of reaction after 100 hours is approximately the same for the same green density (Table 12).

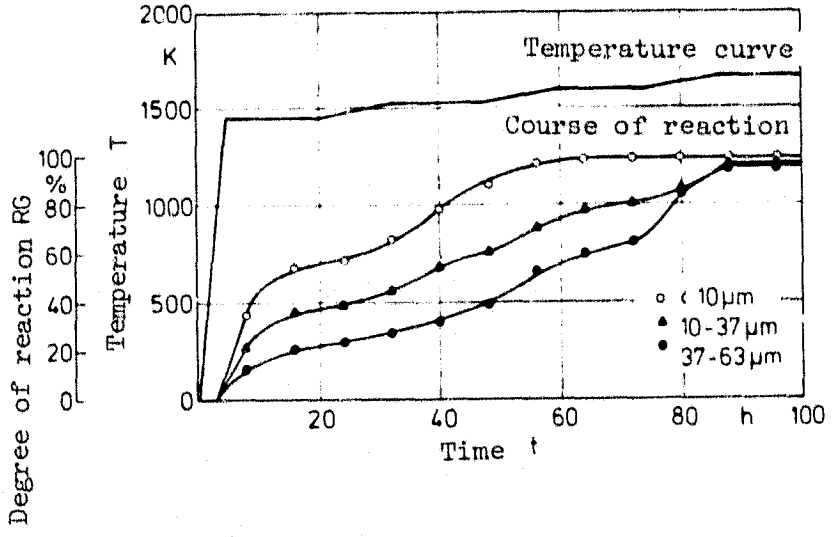

Figure 31. Course of reaction of RSSN with use of different initial silicon particle sizes.

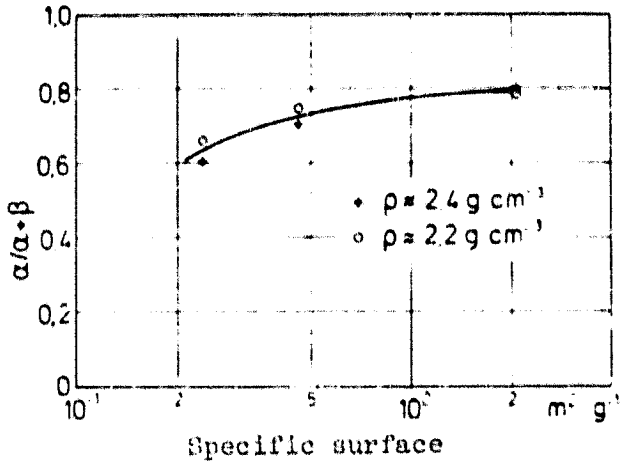

Figure 32. Proportion of α as a function of the specific surface of the initial silicon powder.

4.4.2. Structure analysis

The reason for the increasing degree of reaction with diminishing initial silicon particle size at low nitriding temperatures is based on the higher evaporation rate of silicon due to the increasing specific surface of the powder. As the α phase is presumed to originate through gas phase reactions between Si or SiO and N_2 [21, 25, 42, 73, 119] we would expect here that the volume proportion of the α modification would increase with increasing specific surface (see [119, 120]). Figure 32 shows this rise in α content with increasing specific surface of silicon powder for both series of samples. As shown under 4.3, here too the micropore diameter, D_{50} micropores, determined in the pressure porosimeter decreases with rising α content (Table 12).

Figure 33 shows the porous α mat and the relatively dense areas of the β phase, using as examples the samples with a final density of 2.41 g cm^{-3} (produced from powder A) and 2.38 g cm^{-3} (produced from powder C); see also Table 12.

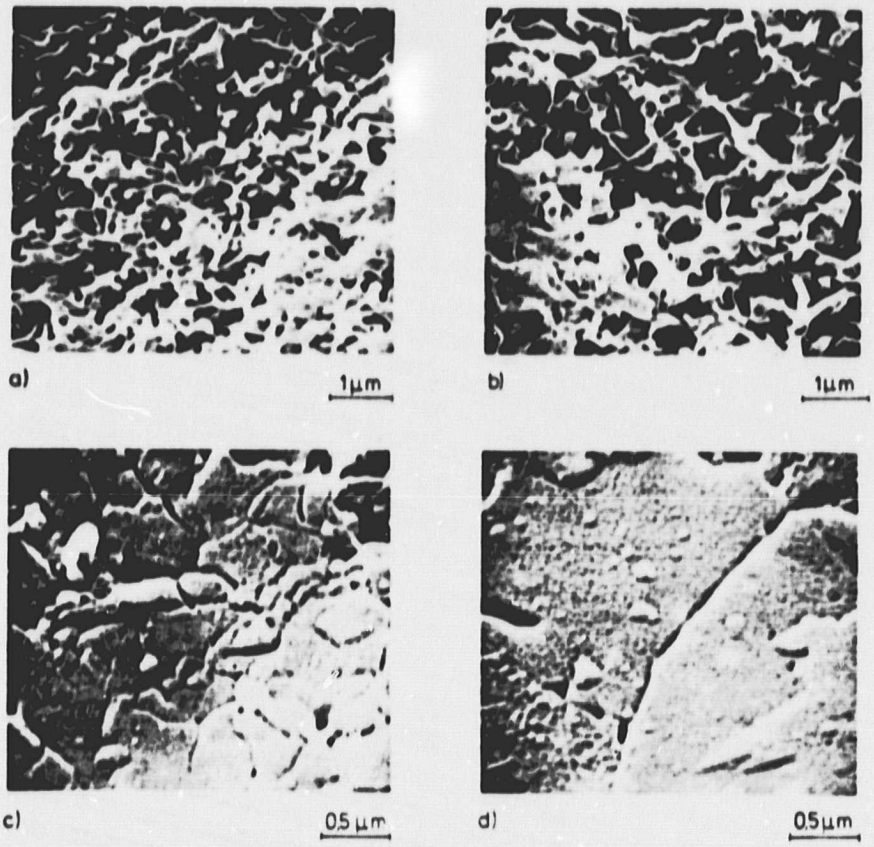

Figure 33. Development of structure in RSSN with use of different initial silicon particle sizes (scanning electron microscope, ground sections, etched).

a) α phase (initial silicon particle size < 10 µm)
b) α phase (initial silicon particle size 37 - 63 µm)
c) β phase (initial silicon particle size < 10 µm)
d) β phase (initial silicon particle size 37 - 63 µm)

Growth of the α needles during nitriding is inhibited during nitriding if either the reaction partners ($Si_{(g)}$ or $SiO_{(g)}$ and $N_{2(g)}$) are no longer available, or if the needles mutually interfere. As the pores with use of powder C are larger than with powder A (Table 12), larger α whiskers can arise (Figure 33). Because of the larger crystallite size, the distribution function of the newly formed micropores in the α phase are shifted to larger d values (Table 12).

With nitriding temperatures below 1673°K the β phase is formed by the reaction of nitrogen with the remaining solid silicon particles [42, 51]. The grain size of the equiaxial β grains increases with increasing initial silicon particle size (Figure 33c and d). As the silicon powder particles can consist of several crystallites, the β crystals can be smaller than the initial silicon particle size in spite of the volume expansion during nitriding. The TEM pictures of the same samples, in Figure 34, also show the α mat with the micropores and the relatively large β grains. They confirm qualitatively the results of the SEM pictures.

Figure 35 shows the light-microscopic pictures from both sample series. With increasing initial silicon particle size the macropore diameter increases. The value for d_{50} macropores determined from these pictures shows that the macropore diameter increases with decreasing final density. With lower green density the pores must be larger than at higher green density for the same initial silicon powder. For a constant volume increase of 22% during nitriding, then, the macropore diameters in the final nitrided samples must also be larger. The individual structure parameters are tabulated once more in Table 12.

4.4.3. Bending strength

Figure 36 shows the curve of bending strength for different initial particle sizes and different densities. As the initial silicon particle size decreases, the parameters which determine the bending strength, such as the grain size, micropore and macropore diameters all decrease, with the resulting increase in bending strength at constant density. We also see here the previously noted increase in strength with increasing density for all three starting powders used.

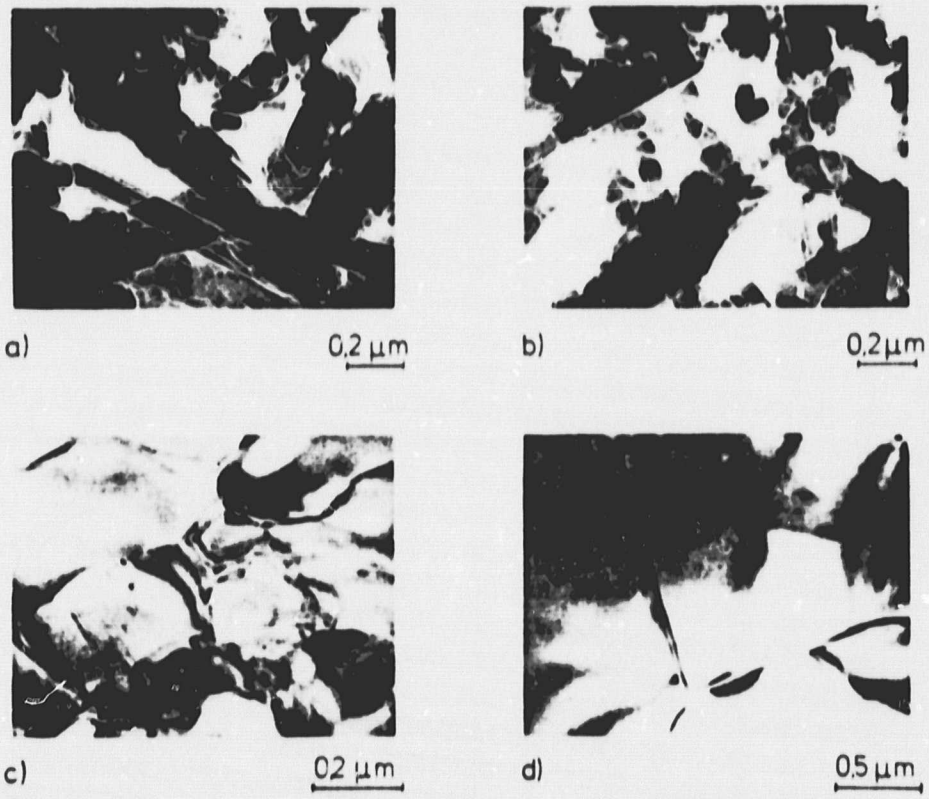

Figure 34. Structural development of RSSN with use of different initial silicon particle sizes (TEM, ion-thinned).

a) α phase (initial silicon particle size < 10 µm)
b) α phase (initial silicon particle size 37-63 µm)
c) β phase (initial silicon particle size < 10 µm)
d) β phase (initial silicon particle size 37-63 µm)

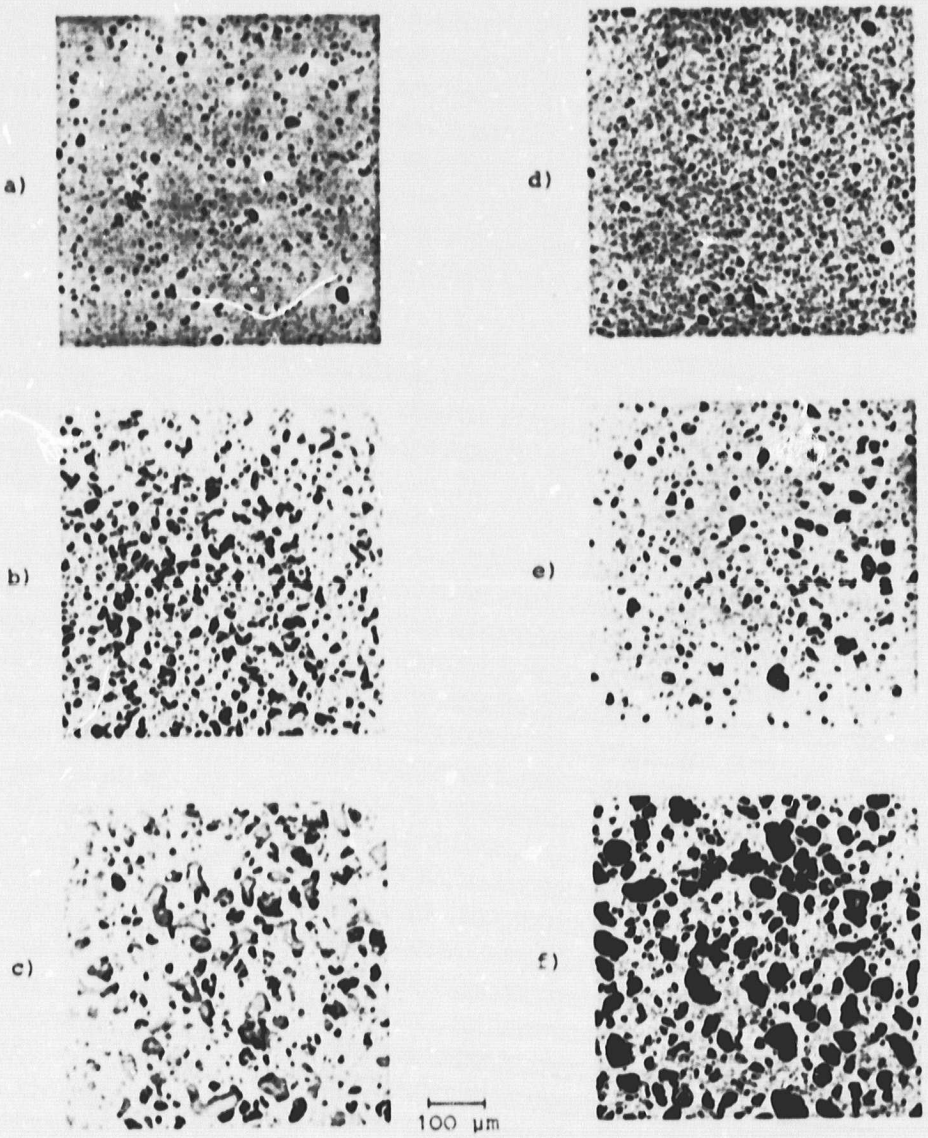

Figure 35. Structural development of RSSN with use of different initial silicon particle sizes (light microscopy, ground sections, etched).

a) $\rho = 2.25$ g cm^{-3} (initial silicon particle size < 10 µm)
b) $\rho = 2.17$ g cm^{-3} (initial silicon particle size 10-37 µm)
c) $\rho = 2.23$ g cm^{-3} (initial silicon particle size 37-63 µm)
d) $\rho = 2.41$ g cm^{-3} (initial silicon particle size < 10 µm)
e) $\rho = 2.42$ g cm^{-3} (initial silicon particle size 10-37 µm)
f) $\rho = 2.38$ g cm^{-3} (initial silicon particle size 37-63 µm)

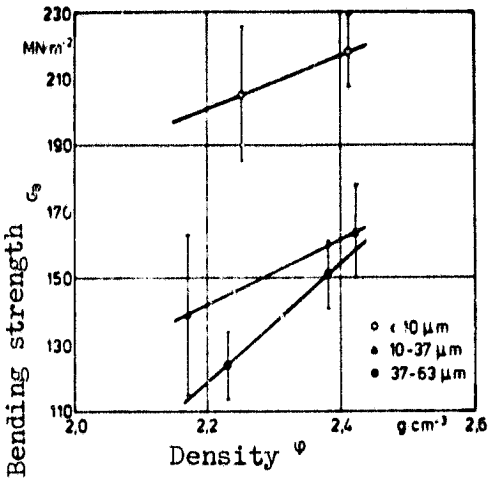

Figure 36. Bending strength as a function of the density and of the initial particle size.

4.4.4 Creep behavior.

Figure 37 shows the course of total elongation versus time at 1573°K and 70 MN m^{-2} for the sample series having a density of 2.4 g cm^{-3}. The creep rate (slope of the curves at 80 hours) increases with increasing initial particle size, from $3.3 \cdot 10^{-6}$ hr^{-1} (< 10 µm) to $8.3 \cdot 10^{-6}$ hr^{-1} (37-63 µm). Steady creep rate does not appear here any more than in the curves in Figures 21, 25 and 29.

As the initial silicon particle size increases, both the micropores and the macropores become larger (Table 12). This makes a large change in the oxidation behavior of these samples. Figure 38 shows the weight increase versus time for heating to incandescence in air at 1573 °K. With increasing initial particle size, that is, for larger pore diameters, the weight increase is considerably greater (proportion of open porosity: < 10 µm, 7%; 10 - 37 µm, 7%; 37-63 µm, 13%). While the material with fine pores (< 10 µm) has already formed

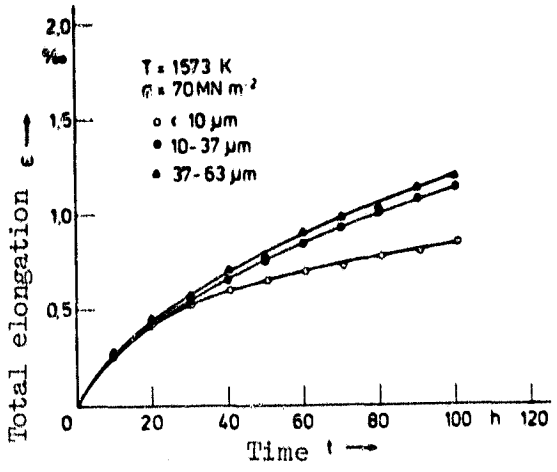

Figure 37. Creep curves of RSSN with different initial silicon particle sizes in air at 1573°K and 70 MN m^{-2}.

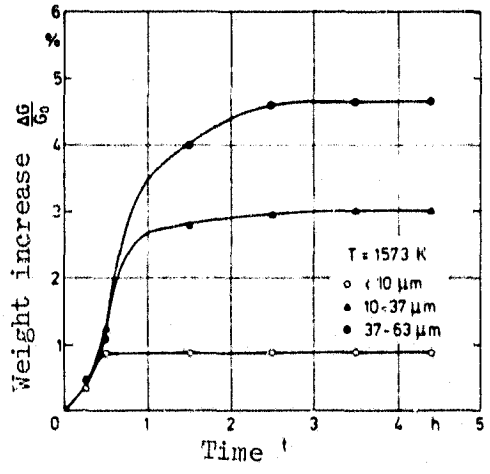

Figure 38. Oxidation curves of RSSN with different initial silicon particle sizes at 1573°K in air.

Table 12. STRUCTURAL PARAMETERS OF RSSN WITH USE OF DIFFERENT INITIAL SILICON PARTICLE SIZES.

Starting powder	Particle size (μm)	Green density ($g \cdot cm^{-3}$)	Final density ($g \cdot cm^{-3}$)	Degree of reaction (%)	$\alpha/\alpha+\beta$	d_{50} micro-pores ($\mu m \cdot 10^{-1}$)	d_{50} macro-pores (μm)	grain size α	grain size β
A	< 10	1,50	2,41	89,9	0,82	0,58	7		
B	10 - 37	1,52	2,42	91,0	0,70	1,08	19		
C	37 - 63	1,48	2,38	93,0	0,60	1,52	28		
A	< 10	1,40	2,25	97,3	0,78	1,30	8		
B	10 - 37	1,38	2,17	96,8	0,75	2,40	22		
C	37 - 63	1,39	2,23	96,8	0,66	2,50	34		

Increasing tendency →

Increasing tendency →

a protective SiO_2 layer after half an hour, which strongly inhibits further oxidation, indicated by proceeding increase in weight. This result again suggests that the internal oxidation of the samples very substantially affects the creep behavior; that is, the formation of the amorphous grain boundary phases due to increased internal oxidation reduced the creep resistance.

4.4.5. Thermal shock behavior

Figure 39 shows the dependence of the bending strength on the quenching temperature difference for oil and water quenching with the samples listed in Table 12 (sample dimensions 3.4 x 3.4 x 45 mm). Here the samples in Figure 39d and f show a considerably lower initial strength in comparison with the results listed in Table 12. Both series of samples were injection-molded simultaneously with those studied in 4.4.3, but only outgassed and nitrided six months later. These samples showed inhomogeneities, which are conjectured to have been caused by changes in the sample bodies during storage, producing the drop in strength.

As observed in 4.2.4, here too we saw no drop in strength until ΔT_c = 1400°K. For water quenching, the critical temperature difference remains nearly constant with increasing initial silicon particle size at a density of $\sim$ 2.2 g cm^{-3}. At a density of $\sim$ 2.4 g cm^{-3}, on the other hand, variations of 87 °K occur in ΔT_c. No systematic relationship can be detected (Figure 39; Table 13). From these results it becomes clear that along with the pore size (and with that, the strength) the other structural parameters also must have a very significant effect on the thermal shock behavior. The E modulus and the transverse contraction number show no systematic changes in both series of samples, while the heat conductivity increases strongly with increasing initial silicon particle size (Table 13). The thermal shock parameter, R', (see 4.2.4), in which not only the strength, the transverse

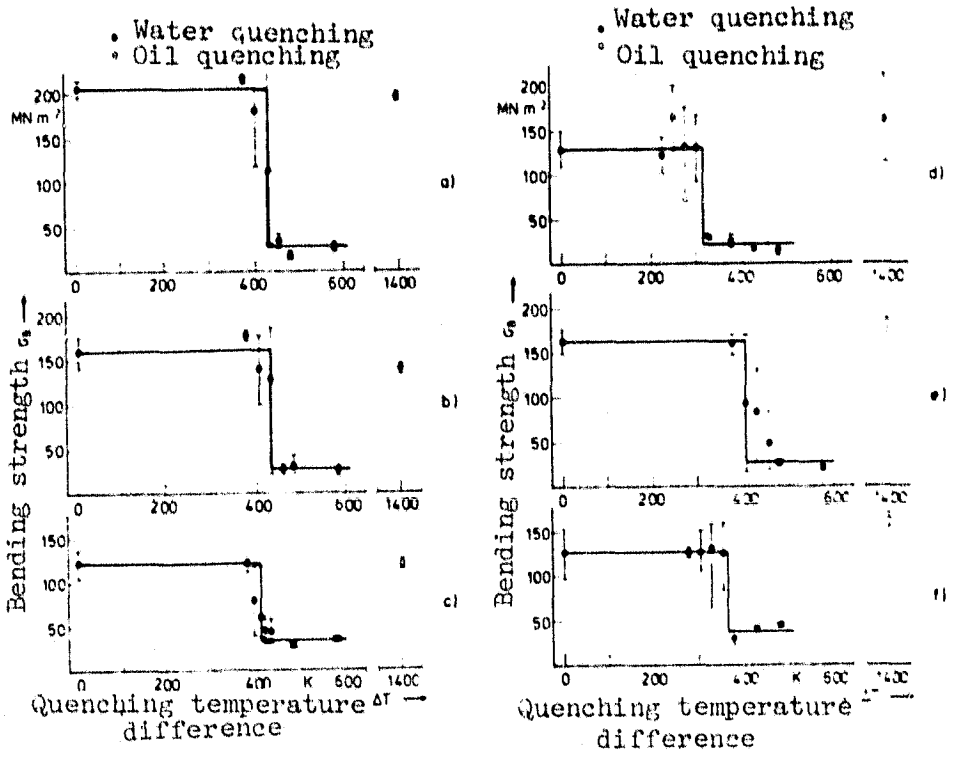

Figure 39. Bending strength as a function of the quenching temperature difference for samples with different initial silicon particle size (single shock, quenching medium water or oil.)

a) ρ = 2.25 (initial silicon particle size < 10 µm)
b) ρ = 2.17 (initial silicon particle size 10 - 37 µm)
c) ρ = 2.23 (initial silicon particle size 37 - 63 µm)
d) ρ = 2.41 (initial silicon particle size < 10 µm)
e) ρ = 2.42 (initial silicon particle size 10 - 37 µm)
f) ρ = 2.38 (initial silicon particle size 37 - 63 µm)

contraction, the elongation coefficients and the E modulus as well as the thermal conductivity are considered, described the experimental results quite well in contrast to R. The increase in strength with decreasing pore size in the sample series with $\rho \approx 2.2\ g.cm^{-3}$, and the increase of ΔT_c, expected from 4.2.4, is compensated by the drop in thermal conductivity with decreasing initial silicon particle size.

Table 13. PHYSICAL PROPERTIES, THERMAL SHOCK PARAMETERS AND CRITICAL TEMPERATURE DIFFERENCE FOR SAMPLES WITH DIFFERENT INITIAL SILICON PARTICLE SIZE AND DENSITY.

Silicon particle size (μm)	ρ ($g \cdot cm^{-3}$)	E ($GN \cdot m^{-2}$)	$1-\nu$	a ($cm^2 \cdot sec^{-1}$)	λ ($Wm^{-1}K^{-1}$)	R (K)	R' (Wm^{-1})	ΔT_c (K)	Relative Values R'	Relative Values ΔT_c
< 10 um	2,25	139	0,80	0,095	14,9	358	5330	425	1	1
10 - 37 um	2,17	127	0,77	0,125	18,9	255	4830	425	0,91	1
37 - 63 um	2,23	133	0,76	0,158	24,5	215	5260	400	0,99	0,94
< 10 um	2,41	171	0,77	0,91	15,3	205	3130	313	0,74	0,78
10 - 37 um	2,42	160	0,78	0,104	17,3	242	4240	400	1	1
37 - 63 um	2,38	154	0,76	0,125	20,7	190	3930	363	0,93	0,91

Also, in the sample series with $\rho \approx 2.4\ g \cdot cm^{-3}$ the experimental results are very well described by R', therefore with consideration of the thermal conductivity. No systematic relation could be detected between ΔT_c or R' and the total porosity from these results.

4.5 Effect of the nitriding gas composition

In this section we shall investigate the effect of hydrogen and argon in the reaction gas on the nitriding reaction, on the structure, and on the bending strength. For this purpose, samples were molded using powder D at constant green density of $1.56\ g \cdot cm^{-3}$, and nitrided with the same temperature-time program and constant total pressure of 950 mbar. The proportions of hydrogen or argon in the nitriding gas were varied from 0 to 20% by volume.

4.5.1. Course of the reaction

Figures 40 and 41 show the temperature-time program and the course of reaction with addition of H_2 and argon, respectively. With increasing hydrogen content, the degree of reaction increases strongly at relatively low nitriding temperatures. With addition of argon, in comparison, there is no effect at all on the course of the nitriding reaction. The curve shape for addition of 20% argon by volume practically matches that for pure nitrogen. The degree of reaction is equal within the individual sample series.

The fact that the degree of reaction in the argon sample series after completion of the nitriding cycle is greater over-all than for the hydrogen-nitrided samples (Figures 40 and 41, Table 14) is very probably not due to the additives to the gas, as the degree of reaction for the samples nitrided in pure nitrogen, in Figure 41, is likewise higher than for the samples in Figure 40. A new powder charge from the

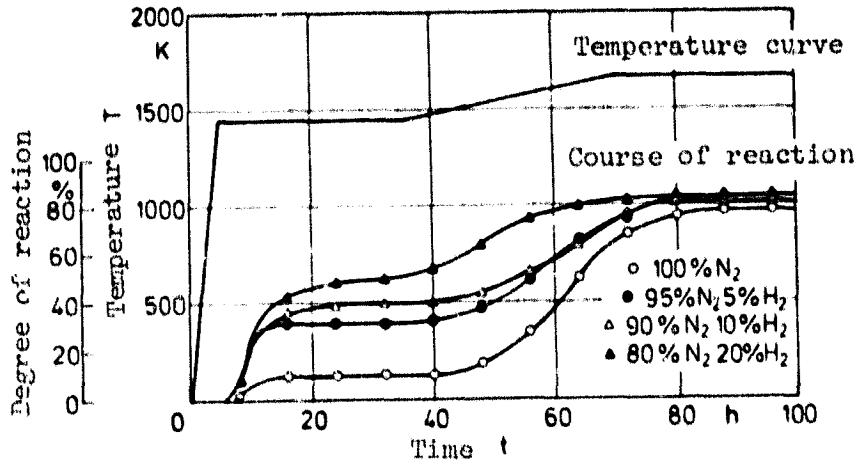

Figure 40. Course of reaction for different N_2:H_2 ratios in the nitriding gas.

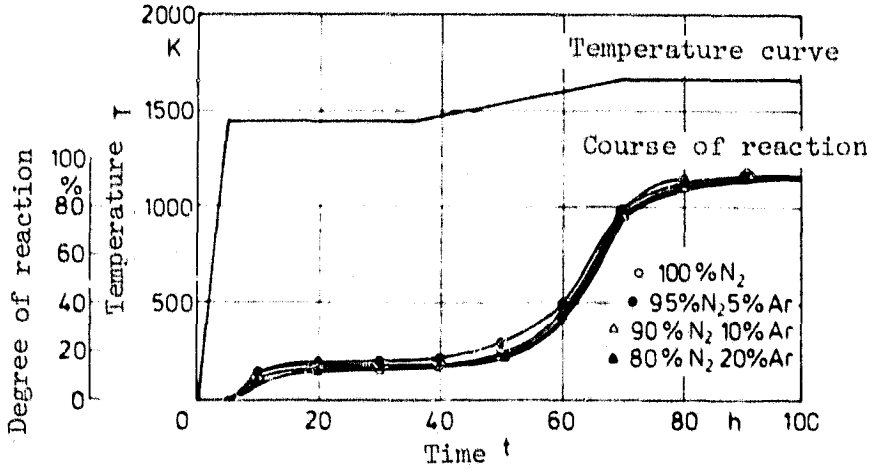

Figure 41. Course of reaction for different N_2:Ar ratios in the nitriding gas.

manufacturer was used for the argon series. Although it had the same particle size distribution, we conjecture a higher proportion of impurities which can lead to an increase in the degree of reaction due to increased formation of low-melting eutectics [114, 115].

The increase of the degree of reaction in the initial stage of the nitriding reaction when hydrogen is added can be explained with the observations made in [121], that hydrogen strongly promotes the formation of SiO in the early stage of nitriding. Then SiO reacts with N_2 forming α-Si_3N_4 with liberation of oxygen. Dervisbegovic [122] also noted an increase in the degree of reaction with addition of hydrogen at the beginning of the nitriding reaction. He found that the reaction

(25) $$3SiO_{(g)} + 2N_{2\,(g)} \rightleftharpoons \alpha\text{-}Si_3N_{4\,(s)} + \tfrac{3}{2}O_{2\,(g)}$$

proceeds toward the right if the partial pressure of oxygen is less than the value of 10^{-17} bar, and this can be attained by addition of hydrogen.

The results in Table 14 show that here too the increase of the degree of reaction with increasing hydrogen content in the nitriding gas at the beginning of the nitriding reaction is linked with an increase in the α content.

4.5.2. Structure analysis

Scanning electron microscope pictures of fracture surfaces show that the structure becomes more finely porous and homogeneous with increasing hydrogen content (Figure 42). Along with the macropore diameter, the micropore diameter also decreases, due to the rising α content, with increasing percentage of H_2 (Table 14; see 4.3 and 4.4). With addition of argon, on the contrary, all the structural parameters listed in Table 14 remain constant. The higher density of the argon sample series is due to the higher degree of reaction (see 4.5.1).

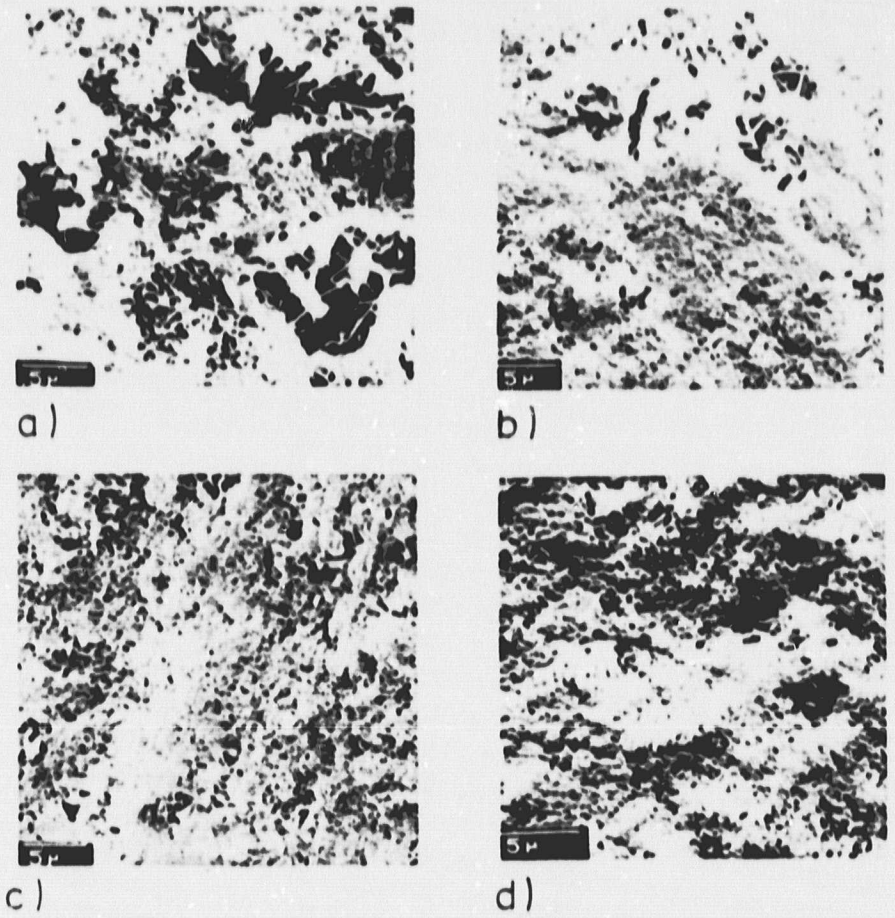

Figure 42. Structural morphology as a function of the composition of the nitriding gas (SEM, fracture surfaces).

a) $N_2:H_2$ = 100:0 (% by volume)
b) $N_2:H_2$ = 95:5 (% by volume)
c) $N_2:H_2$ = 90:10 (% by volume)
d) $N_2:H_2$ = 80:20 (% by volume)

4.5.3. Bending strength

Figure 43 shows the curve for strength as a function of the different additions to the nitriding gas. The addition of argon causes no structural changes in the samples, so that the strength remains constant. In contrast, the strength for addition of 10% H_2 by volume increases from 162 MN m^{-2} (100% N_2) to 204 MN m^{-2}. This increase can be explained as due to the more homogeneous structure (Figure 42; Table 14). With an

addition of 20% hydrogen by volume the strength falls again. This drop in strength cannot be explained with the analytical values now available. Mangels [71] also found a maximum in the strength, although he found it using only 1% H_2 in the

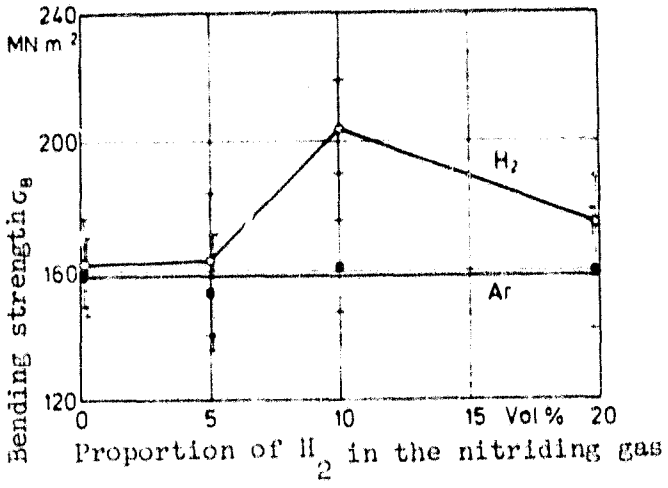

Figure 43. Dependence of the bending strength on the nitriding gas composition.

nitriding gas. To be sure, he used a mullite tube furnace, as a variation from the experiments conducted here, which might have changed the gas composition. In addition, the final temperature was not 1673°K as here, but 1773°K. Jones and Lindley [123] who like Gugel et al. [124] were unable to confirm this dependence, related the strength maximum found by Mangels to the fact that he nitrided at temperatures above the melting point of silicon (1683°K). They explained the differing results to the drop in strength found with nitriding temperatures above the melting point of silicon. Use of hydrogen in the nitriding gas caused a large part of the reaction to occur at lower temperature, as we observed also (Figure 40), so that the rise in strength observed by Mangels may have been a result of the degree of conversion below the melting point of silicon. The present investigations, though, have shown that

Table 14. STRUCTURAL PARAMETERS OF RSSN AFTER NITRIDING WITH DIFFERENT NITRIDING GAS COMPOSITION

$N_2:H_2$ (% vol.)	Degree of reaction (%)	ρ (g cm^{-3})	$\alpha/\alpha+\beta$	d_{50} micropores ($\mu m \cdot 10^{-1}$)	d_{50} macropores (μm)
100: 0	77,9	2,39	0,51	0,86	22
95: 5	83,9	2,45	0,67	0,70	20
90:10	80,9	2,42	0,69	0,60	12
80:20	83,0	2,45	0,77	0,50	12
N_2:Ar [Vol.%]					
100: 0	91,5	2,53	0,44	0,91	21
95: 5	92,6	2,54	0,47	0,89	20
90:10	92,1	2,54	0,47	0,92	23
80:20	92,5	2,54	0,47	0,90	20

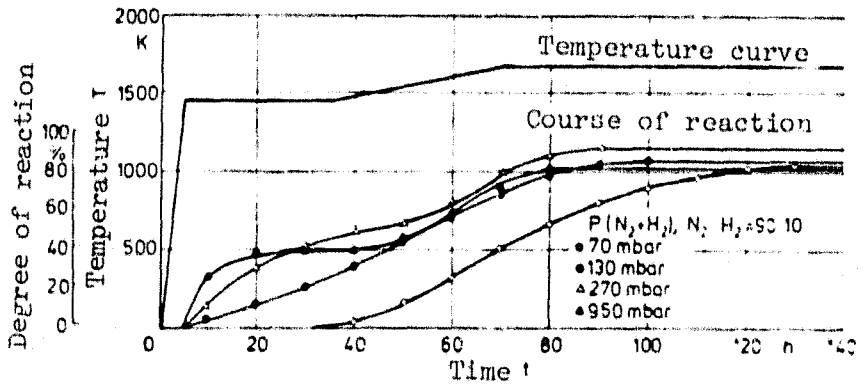

Figure 44. Course of reaction at different nitrogen partial pressures.

a maximum occurs in the strength even if the entire nitriding reaction proceeds below the melting point of silicon.

4.6 Effect of the nitriding gas pressure

In the previous section, of course, the partial pressure of nitrogen was slightly reduced by addition of hydrogen or argon. In the following, though, the course of nitriding is studied, and the structure and strength are examined, if the nitrogen partial pressure decreases to 70 mbar during the nitriding. For this, the samples used had a green density of 1.59 g cm^{-3} and were nitrided in a mixture of N_2, H_2 and Ar. The ratio N_2:H_2 was always 90:10. The partial pressure of the (N_2 + H_2) mixture was reduced from 950 mbar to 70 mbar (Table 15). The total pressure was always kept constant by addition of argon (950 mbar).

4.6.1 Course of the reaction

Figure 44 shows the temperature-time program and the course of the reaction for various nitrogen partial pressures. As the nitrogen partial pressure is reduced the reaction rate decreases strongly. This automatically increases the reaction time required to attain a comparable degree of reaction.

4.6.2. Structure analysis

Table 15 shows the change of the individual structural parameters with decreasing nitrogen partial pressure. Both the micropore diameter and the macropore diameter increase with decreasing nitrogen partial pressure. Figure 45 shows sections of the fracture surfaces from samples with different N_2 pressures. As the N_2 pressure decreases, the structure becomes more grossly porous and less homogeneous. This coarsening of the structure was also described by Atkinson et al. [49]. According to their

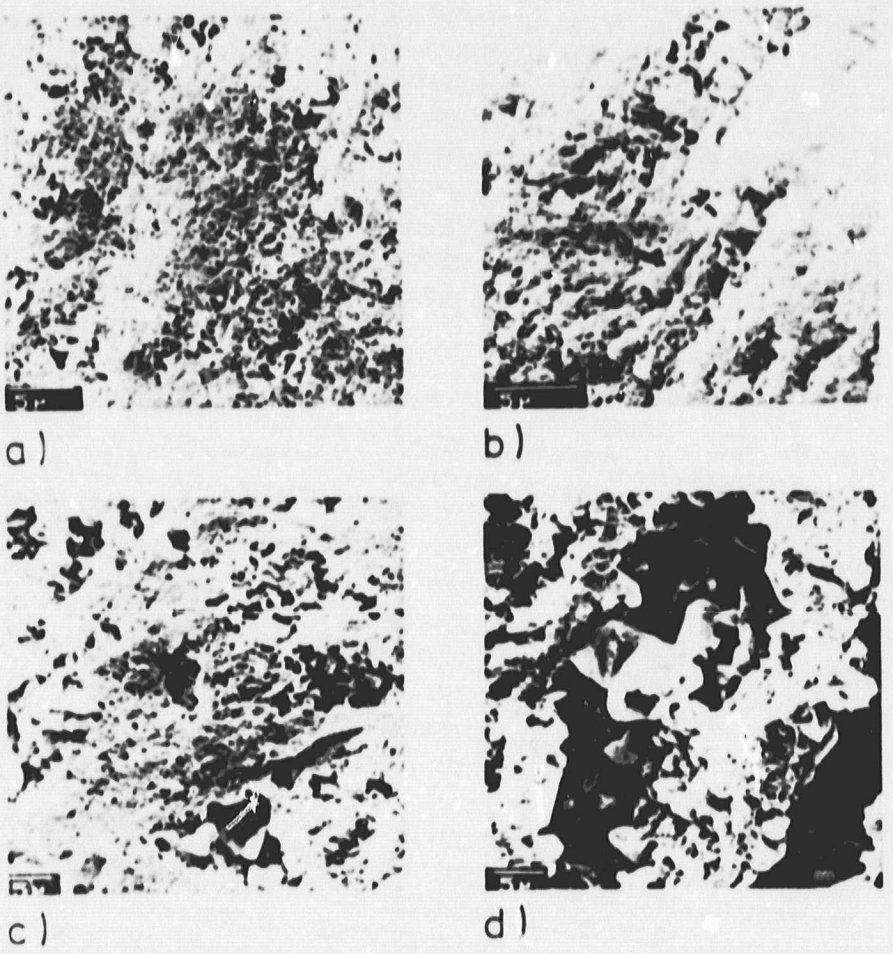

Figure 45. Structural morphology as a function of the nitriding gas partial pressure (SEM, fracture surfaces).
a) 950 mbar b) 270 mbar c) 130 mbar
d) 70 mbar
$N_2:H_2$ = 90:10

concept the homogeneous structure at high nitrogen partial pressure results from the large number of Si_3N_4 nuclei forming, which cause a finely granular or finely porous structure. On the contrary, at low N_2 pressures, relatively few Si_3N_4 nuclei form on the silicon surface. With the advance of the reaction, nitrogen evaporates at the still uncoated surfaces

Table 15. STRUCTURAL PARAMETERS OF RSSN AFTER NITRIDING AT VARYING NITROGEN PARTIAL PRESSURES

$P_{(N_2+H_2)}$ [mbar]	RG [%]	ρ [$g \cdot cm^{-3}$]	$\alpha/\alpha+\beta$	d_{50} macropores [$\mu m \cdot 10^{-1}$]	d_{50} micropores [μm]
950	89,6	2,50	0,60	0,55	21
270	92,4	2,53	0,64	1,58	27
130	85,7	2,49	0,45	·,60	40
70	84,5	2,42	0,57	17,0	42

and deposits on or diffuses to the few nuclei. As the individual nuclei are more separated at lower pressures than at higher pressures, the higher pressures give a finer and more homogeneous structure, as is also observed here. This mechanism also explains the decrease in reaction rate with decreasing nitrogen partial pressure in the nitriding gas.

4.6.3 Bending strength

Figure 46 shows the dependence of the bending strength on the nitrogen partial pressure in the nitriding gas. As was to be expected, the strength decreases with decreasing N_2 pressure because of the related coarsening in structure; that is, because of the increase in micropore diameters. The total porosity will also have a smaller effect in this drop in strength, because as a result of the lower degree of reaction in the samples nitrided at 70 mbar the density is somewhat lower than at the higher pressures (Table 15).

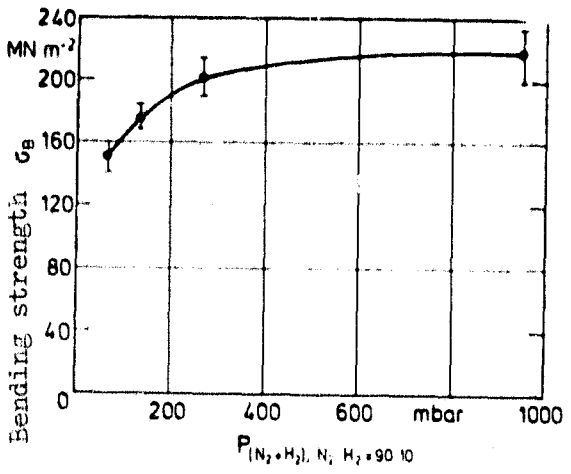

Figure 46. Effect of the nitrogen partial pressure during nitriding on the bending strength.

5. General discussion and conclusions

For most mechanical properties of RSSN it is desirable to have homogeneous structure and the minimum of porosity. With the production technologies available today, the minimum attainable total porosity of RSSN is about 15%. We must, then, attempt further optimization of the structure by varying the production conditions. By using silicon particle feedstocks with optimal spherical packing and high specific surface the pore size distribution can be shifted toward smaller diameters (macropores) in the 'green state' and, therefore, also after nitriding. As the α modification is believed to be produced via the gas phase (see 2.3), and more gaseous Si or SiO is available for reaction with higher specific surface, the α proportion increases and the micropore radius decreases (See 4.4).

One can see a further homogenizing effect on structure development with use of hydrogen in the nitriding gas. Because of the thermodynamic instability of silicon in air there are practically always SiO_2 layers on the surface of silicon particles. With hydrogen present the oxygen partial pressure in the nitriding gas is reduced. Thus, SiO_2 can be reduced to SiO and react with nitrogen, forming α-Si_3N_4 [112, 122]. This can also reduce the size of the macropores (see 4.5) as well as reducing the micropore diameter.

Another possible way of optimizing the structural parameters with respect to improving the mechanical properties is increasing the nitrogen pressure during nitriding. In agreement with the model concepts of Atkinson, Moulson and Roberts [49], it can be shown from the course of the reaction and the structural analyses that, because of the low number of Si_3N_4 nuclei which form, the reaction rate of nitriding decreases with low nitrogen partial pressures, producing a very inhomogeneous coarsely porous structure (see 2.4 and 4.6). That is, a high nitrogen pressure during nitriding is necessary to produce homogeneous finely porous structures.

The present state of development does not yet appear to have arrived at the end of exploitable possibilities for optimizing the material qualities of RSSN materials with respect to their use as design materials. Nitriding at pressures of several thousand $MN \cdot m^{-2}$ is already being considered to produce materials of higher density than attainable now with very homogeneous structure. Attempts should also be made to optimize the structure and mechanical properties by use of very fine silicon powder in the submicron range. Admittedly, this would give problems in process control because of the exothermy of the conversion reaction; and such powders are very difficult to process, particularly with the injection molding technology. But even for the RSSN materials available today it seems possible to improve the mechanical properties

and the oxidation behavior, which is particularly important for creep behavior, by appropriate aftertreatment. One possibility is that of coating with α-Si_3N_4 by the CVD process.

In considering the room temperature bending strength of RSSN as a function of the total porosity (or of the density), the great scattering at the same porosity is striking in comparison with measurements reported in the literature (Figure 47).

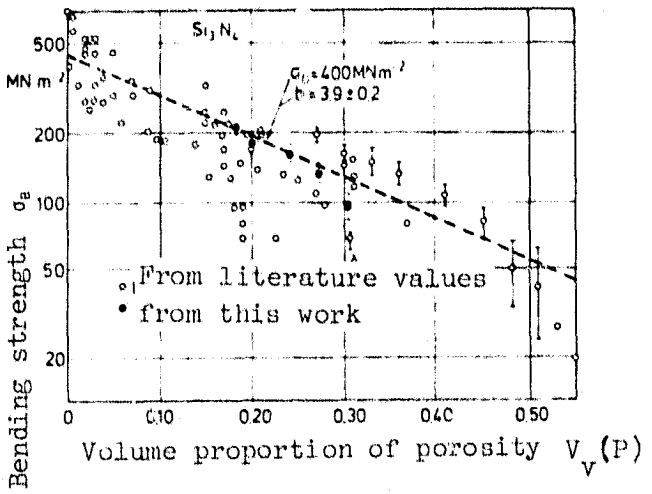

Figure 47. Dependence of the bending strength on the porosity (from [65]).

In many cases, to be sure, including in this work, the dependence of the bending strength on the total porosity can be described by an exponential function. The strength increases with decreasing porosity, but to some extent the variance of the constants of these functions differ substantially [46, 65] (see 4.1.1). One reason for this could be that materials having different structural parameters with the same total porosity are being compared.

Fracture-mechanical considerations show that at constant porosity the room temperature strength of brittle materials is principally influenced by the fracture toughness and the critical crack size, a (Equation (22)):

$$\sigma_B = \frac{K_{Ic}}{\sqrt{a}\, Y} = \sqrt{\frac{2\,\gamma\,E}{a}}\,\frac{1}{Y} \cdot \tag{22}$$

This appears especially with variation of the macropore diameter at constant total porosity. While the K_{Ic} factor remains practically unaffected by the pore size distribution, the pore size changes. This can be considered as the critical crack size, so that with the same total porosity the strength varies as $\sigma \sim a^{-1/2}$ (see 4.2.2). Along with the macropore size, the strength is also affected by the proportion of the α modification, or by the new micropores which originate with nitriding, so that the strength increases with increasing proportion of α or with decreasing micropore diameter. The increase in strength with increasing α proportion has also been reported by Jennings et al. [74]. In their work, apparently because of the production conditions, the size of the micropores decreased and no prediction was made. In order to study the effect of the total porosity on the room temperature strength one should, according to these concepts, use only samples having a constant α proportion and the same pore size distribution with different porosities. As this requirement cannot be fulfilled in practice because of the complex processes in production of RSSN, and the structural parameters can vary strongly due to different preparation conditions (see 4.4 to 4.6), the scattering of strength with the same total porosity in Figure 47 is understandable.

The maximum attainable density (or minimum porosity) of RSSN is limited due to the manner of production, so that the structure must be optimized for further increase in strength. That is, essentially the critical crack size must be reduced. Therefore, to produce RSSN grades with high

strength, it is necessary to have not only minimum porosity but homogeneous and very finely distributed pores.

Structural changes also appear very noticeably in the study of the creep behavior. For instance, the creep rate shows the quadratic dependence on the total porosity which has been found with other ceramic materials. This relation, though, applies only for samples which were produced from the same silicon powder with constant nitriding conditions (see 4.1.2.).

As was shown extensively in [80], viscous flow of an amorphous grain boundary phase with accomodation through grain boundary separation or crack formation is the creep mechanism for RSSN, and the oxidation products of Si_3N_4 must be considered the grain boundary phases. But, along with the open porosity, it is principally the size of the micropores which is responsible for the oxidation behavior of RSSN. With very fine micropores, a protective oxide layer can form very quickly on the surface, preventing complete internal oxidation. With large micropores, though, there can be increased internal oxidation (see 4.3.2 and 4.4.4). Thus it is understandable that the creep rate increases with a decrease of the proportion of α in RSSN, as well as with an increase in the initial silicon particle size; both result in enlargement of the micropores and, therefore, increased internal oxidation (see 4.3.2 and 4.4.4). With the same total porosity, for instance, with a change of the value of $\alpha/\alpha+\beta$ from 0.78 to 0.16 (change of the micropore radius from $0.64 \cdot 10^{-1}$ µm to $1.70 \cdot 10^{-1}$ µm) the creep rate increases just as much as with the change in total porosity from 19% to 27% (cf. Figures 21 and 29).

The prerequisite for a creep-resistant RSSN material is, then, as it is for strength, a high α proportion and finely distributed pores with minimum total porosity.

Changes in the structural parameters also result in different thermal shock behavior of RSSN. The observed drop in the critical temperature difference, ΔT_c, with increasing pore size and the other structural parameters constant (see 4.2.4) can be explained on consideration of the fracture mechanical theory of fracture initiation by thermal stresses [87]. With the assumption of a semicircular surface crack, the critical crack size increases correspondingly [125] as:

$$a = 0{,}74 \left(\frac{K_{Ic}}{\sigma_B}\right)^2 \tag{26}$$

Calculation of a according to Equation (26) yielded an increase from 88 µm to 229 µm with increasing pore size and the other structural parameters the same (see 4.2). In agreement with [87], this increase leads to a decrease in ΔT_c, which agrees with the experimental results (see 4.2.4).

We may also make an estimate, from the mechanical and physical properties of the samples, of the maximum critical temperature difference which the samples may be exposed to without damage. When a horizontal circular cylinder is quenched, ΔT_c is given by [126]:

$$\Delta T_c = \frac{1{,}451 \cdot \sigma_B \cdot (1 - \nu)}{\alpha \cdot E} \left(1 + \frac{3{,}41}{\beta}\right) \tag{27}$$

with

$$\beta \text{ (Biot number)} = \frac{d \cdot h}{2 \cdot \lambda}. \tag{28}$$

where d = diameter of the sample
h = heat transport number of the quenching medium.

A crude estimation of β for the given quenching conditions shows that the second term in Equation (27), which also contains the thermal conductivity, cannot be neglected.

This is expressed especially clearly in consideration of the critical temperature difference with samples produced from silicon powders with different initial particle sizes. The value of ΔT_c can remain constant in spite of a large increase in the pore size (and resulting drop in strength) if the thermal conductivity increases simultaneously, as it does here (see 4.4.5).

6. Summary

The effect of the preparation conditions on the structural morphology and the mechanical properties such as the room temperature bending strength, the creep behavior, and the thermal shock behavior were studied with reaction-bonded silicon nitride. The major results can be summarized as follows:

1) The structural parameters can be varied over wide ranges by means of the preparation conditions. At constant total porosity, the following structural changes were observed with decreasing initial silicon particle size:
   The density and, with it, the total porosity and the proportion of free silicon remain unchanged.
   The proportion of the α modification increases.
   The diameters of the newly formed micropores in the α mat and the diameters of the macropores decrease.
   The particle size in the α and β crystallites decreases.

2) Addition of up to 20% argon in the nitriding gas has no effect at all on the structural parameters.
   As the proportion of hydrogen in the nitriding gas increases (up to 20% by volume) the sizes of the micropores and macropores decrease. The α proportion in the samples increases.

3) With decreasing nitrogen partial pressure during nitriding (< 750 mbar) the reaction rate decreases. The diameters of the micropores and macropores increase.

4) With constant preparation conditions, the strength increases exponentially with decreasing total porosity.

5) With constant total porosity and otherwise identical structural parameters the dependence of the strength on the macropore diameters, which act as critical crack sizes, can be described by a power function with an exponent of $-\frac{1}{2}$.

6) With constant total porosity and constant macropore size distribution, the $\alpha/\alpha+\beta$ ratio is varied by heating above the melting point of silicon. The strength decreases with increasing β proportion or increasing micropore radius.

7) At constant preparation conditions the creep rate rises as the square of the total porosity.

8) At constant total porosity the size of the micropores and, with it, the oxidation behavior have a very strong effect on the creep rate. With small micropore diameters a protective SiO_2 layer forms relatively quickly on the outside of the samples at high temperatures (1573 °K), preventing further oxidation. With larger micropores, in contrast, there is increased internal oxidation of the samples. Material grades with large micropore diameters and, therefore, greater internal oxidation, show a considerably higher creep rate than those with small micropore diameters.

9) The macropore size and thermal conductivity largely determine the thermal shock behavior of RSSN. With constant total porosity and otherwise identical structural parameters the critical temperature difference, which is a measure of resistance to thermal shock, increases with decreasing macropore size and, thus, with increasing strength.

10) In spite of the increase in the pore size, the critical temperature difference can remain constant if the thermal conductivity rises simultaneously due to variation of other structural parameters. The thermal shock behavior can be described well by the thermal shock parameter R', which takes into consideration not only the strength but also the E-modulus, transverse contraction number, the thermal expansion coefficient and the thermal conductivity.

This work originated from the Institute for Materials Research of the German Research and Experimental Establishment for Air and Space Travel at Cologne.

I thank Prof. Dr. H. Hausner for stimulation, support, and scientific monitoring of this work.

I thank Prof. Dr. W. Bunk for valuable suggestions and promotion of this work.

I also thank Dr.-Ing. M. Böhmer, Dr.-Ing. H. Knoch, Dr. D. Munz, Dr.-Ing. G. Streb and Dr.-Ing G. Ziegler for many interesting suggestions and councils.

I heartily thank J. Hermanns, who supported me in the performance of this work. My special thanks go to my coworkers at the institute who contributed to the success of the work.

REFERENCES

[1] Turkdogan, E. T., Bills, P. M., Tipett, V. A.: Silicon Nitrides: Some Physicochemical Properties. J. Appl. Chem. 8 (1958), p. 296-302.

[2] Hardie, D., Jack, K. H.: Crystal Structure of Silicon Nitride. Nature 180 (1957), p. 332-333.

[3] Ruddlesden, S. N., Popper, P.: On the Crystal Structure of the Nitrides of Silicon and Germanium. Acta Cryst. 11 (1958), p. 465-468.

[4] Wild, S., Grieveson, P., Jack, K. H.: The Crystal Structures of Alpha and Beta Silicon and Germanium Nitrides. Special Ceramics 5 (1972), p. 385-395.

[5] Forgeng, W. D., Decker, B. F.: Nitrides of Silicon. Trans. Metal. Soc. AIME 212 (1958), p. 343-348.

[6] Narita, K., Mori, K.: Crystal Structures of Silicon Nitride. Bull. Chem. Soc. Japan 32 (1959), p. 417-419.

[7] Kaiser, W., Thurmond, C. D.: Nitrogen in Silicon. J. Appl. Phys. 30 (1959), p. 427-431.

[8] Popper, P., Ruddlesden, S. N.: The Preparation Properties and Structure of Silicon Nitride. Trans. Brit. Ceram. Soc. 60 (1961), p. 603-626.

[9] Suzuki, H.: The Synthesis and Properties of Silicon Nitride. Bull. Tokyo Inst. of Tech. No. 54 (1963), p. 163-177.

[10] Thompson, D. S., Pratt, P. L.: The Structure of Silicon Nitride. Science of Cramics 3 (1967), p. 33-51.

[11] Marchand, R., Laurent, Y., Lang, J., LeBihan, M. Th.: Structure of Alpha Silicon Nitride. Acta Cryst. B 25 (1969), p. 2157-2160.

[12] Galasso, F., Kuntz, K., Croft, W. J.: Pyrolytic Si_3N_4. J. Amer. Ceram. Soc. 55 (1972), p. 431.

[13] Priest, H. F., Burns, F. C., Priest, G. L., Skaar, E.: The Oxygen Content of Alpha Silicon Nitride. J. Amer. Ceram. Soc. 56 (1973), p. 395.

[14] Feld, H., Ettmayer, P., Petzenhauser, I.: Oxygen Stabilization of α-Si_3N_4. Ber. Dt. Keram. Ges. 51, (1974), p. 127-131.

[15] Kohatsu, I., McCauley, J. W.: Re-examination of the Crystal Structure of α-Si_3N_4. Mat. Res. Bull. 9 (1974), p. 917-920.

[16] Kato, K., Inoue, Z., Kijiama, K., Kawada, J., Yamane, T., Tanaka, H.: Structural Approach of the Problem of Oxygen Content in Alpha Silicon Nitride. J. Amer. Ceram. Soc. 58 (1975), p. 90-91.

[17] Blegen, K.: Equilibria and Kinetics in the Systems Si-N and Si-N-O. Special Ceramics 6 (1975), p. 223-244.

[18] Jennings, H. M.: An Investigation of the Relationship between Processing Conditions, Microstructure and Mechanical Properties of Reaction Bonded Silicon Nitride. Ph.D.Th., Brown University, Providence, R. I., June, 1975.

[19] Patent specification 1.272.145, May 3, 1972. Plessey Comp. Ltd.

[20] Patent No. 2.147.513, March 30, 1972. Joseph Lucas Ltd.

[21] Messier, D. R., Wong, P.: Kinetics of Nitridation of Silicon Powder. J. Amer. Ceram. Soc. 56 (1973), p. 480-485.

[22] Messier, D. R., Wong, P., Ingram, A. E.: Effect of Oxygen Impurities on the Nitridation of High Purity Silicon. J. Amer. Ceram. Soc. 56 (1973), p. 171-172.

[23] Guthrie, R. B., Riley, F. L.: The Nitridation of Single-Crystal Silicon. Proc. Brit. Ceram. Soc. 22 (1973), p. 278-280.

[24] Lin, S. S.: Mass Spectrometrie Studies of the Nitridation of Silicon. J. Amer. Ceram. Soc. 58 (1975), p. 271-273.

[25] Campos-Loritz, D., Riley, F. L.: The Effect of Silica on the Nitridation of Silicon. J. Mat. Sci. 11 (1976), p. 195-198.

[26] Torre, J. P., Mocellin, A.: Some Effects of Al and O_2 on the nitridation of silicon compacts. J. Mat. Sci. 11 (1976), p. 1725-1733.

[27] Elias, D. P., Lindley, M. W.: Reaction Sintered Silicon Nitride. J. Mat. Sci. 11 (1976), p. 1278-1287.

[28] Cutler, I. B., Croft, W. J.: Silicon Nitride (Part 1). Powd. Met. Intern. 6 (1974), p. 92-96. (Part 2) ibid p. 144-148.

[29] Alliegro, R. A., Richerson, D. W., Torti, M. L., Washburn, M. E., Weaver, G. Q.: Silicon Nitride and Silicon Carbide for High Temperature Engineering Applications. Proc. Brit. Ceram. Soc. 22 (1973), p. 129-146.

[30] Zdaniewski, W., Knoch, H., Heinrich, J., Hasselman, D. P. H.: Effect of Oxidation on thermal Diffusivity of Reaction-Sintered Silicon Nitride. Bull. Amer. Ceram. Soc., accepted for publication.

[31] Godfrey, D. J., Lindley, M. W.: The Strength of Reaction-Bonded Silicon Nitride Ceramics. Proc. Brit. Ceram. Soc. 22 (1973), p. 229-252.

[32] Lange, F. F.: High-Temperature Strength Behavior of Hot Pressed Si_3N_4: Evidence for Subcritical Crack Growth. J. Amer. Ceram. Soc. 57 (1974), p. 84-87.

[33] Washburn, M., Baumgartner, H.: High-Temperature Properties of Reaction-Bonded Silicon Nitride. In: J. J. Burke, A. E. Gorum and R. N. Katz (Herausg.), Ceramics for High Performance Applications, p. 479-492. Chestnut Hill, Mass.: Brook Hill Publishing Co., 1975.

[34] Wirth, G.: The Effect of Oxidation on Hot Bending and Tensile Strength of Reaction-Sintered Silicon Nitrides of Different Types of Manufacture. Werkstoff-Kolloquium der DFVLR, Institut für Werkstoff-Forschung, Porz-Wahn, November 17, 1977.

[35] Heinrich, J., Boehmer, M.: The Effect of Nitriding Conditions on the Structure and Mechanical Characteristics of Reaction-Sintered Silicon Nitride. Forschungsbericht der Deutschen Luft-und Raumfahrt DLR-FB 77-22 (1977).

[36] Heinrich, J.: Effect of the Initial Particle Size of Silicon on the Structure and the Mechanical Characteristics of Reaction-Sintered Silicon Nitride. Ber. Dt. Keram. Ges. 55 (1978) p. 238-241.

[37] Heinrich, J., Streb, G.: Quantitative Microstructural Analysis of Reaction-Bonded Silicon Nitride. J. Mat. Sci., accepted for publication.

[38] Parr, N. L., May, E. R. W.: The Technology and Engineering Applications of Reaction-Bonded Silicon Nitride. Proc. Brit. Ceram. Soc. 7 (1967), p. 81-98.

[39] Evans, A. G., Sharp, J. V.: Microstructural Studies on Silicon Nitride. J. Mat. Sci. 6 (1971), p. 1292-1302.

[40] Evans, A. G., Sharp, J. V.: Electron Microscopy and Structure of Materials, ed. by G. Thomas, R. M. Fulrath and R. M. Fisher (University of California Press), 1972 p. 1141-1154.

[41] Danforth, S. C., Richman, M. H.: Transmission Electron Microscopy of Reaction-Bonded Silicon Nitride. Metallography 9 (1976), p. 321-332.

[42] Jennings, H. M., Richman, M. H.: Structure, Formation Mechanism and Kinetics of Reaction-Bonded Silicon Nitride. J. Mat. Sci. 11 (1976), p. 2087-2098.

[43] Jennings, H. M., Edwards, J. O., Richman, M. H.: Molecular Structure, Microstructure, Macrostructure and Properties of Silicon Nitride. Inorg. Chim. Acta 20 (1976 p. 167-181.

[44] Carr, E. M., Bartlett, R. W.: Technical Report AFML-TR-68-197. (1968).

[45] Gefferkorn, G., Vahl, J.: The Combination of Light Microscopic, Electron Microscopic and X-ray Methods for Study of Metal Oxide Whiskers and Coatings. Werkstoffe und Korrosion 14 (1963), p. 1021-1029.

[46] Thompson, D. S., Pratt, P. L.: The Mechanical Properties of Reaction-Sintered Silicon Nitride. Proc. Brit. Ceram. Soc. 6 (1966), p. 37-47.

[47] Atkinson, A., Leatt, P. J., Moulson, A. J., Roberts, E. W.: A Mechanism for the Nitridation of Silicon Powder Compacts. J. Mat. Sci. 9 (1974), p. 981-984.

[48] Godfrey, D. J.: Ceramics for High-Temperature Engineering. Proc. Brit. Ceram. Soc. 22 (1973), p. 1-25.

[49] Atkinson, A., Moulson, A. J., Roberts, E. W.: Nitridation of High Purity Silicon. J. Amer. Ceram. Soc. 59 (1976), p. 285-289.

[50] Campos-Loritz, D., Riley, F. L.: Factors affecting the Formation of the α- and β-phases of silicon nitride in the nitridation of silicon powders. Science of Ceramics 9 (1977), p. 38-45.

[51] Longland, P., Moulson, A. J.: The Growth of α- and β-Si_3N_4 accompanying the nitridation of silicon powder compacts. J. Mat. Sci. 13 (1978), p. 2279-2280.

[52] Danforth, S. C., Jennings, H. M., Richman, M. H.: The Ladder Microconstituent of Silicon Nitride. Metallorgraphy 9 (1976), p. 361-365.

[53] Metcalfe, B. L.: Comment on the Ladder Phase in Silicon Nitride. Metallorgraphy 11 (1978), p. 231-233.

[54] Mitomo, M.: Effect of Fe and Al Additions on Nitridation of Silicon. J. Mat. Sci. 12 (1977), p. 273-276.

[55] Dawson, W. M., Arundale, P., Moulson, A. J.: Development and Control of Microstructure in Reaction-Bonded Silicon Nitride. Science of Ceramics 9 (1977), p. 111-118.

[56] Boyer, S. M., Moulson, A. J.: A Mechanism for the Nitridation of Fe-contaminated Silicon. J. Mat. Sci. 13 (1978) p. 1637-1646.

C-2

[57] Danforth, S. C.: Fabrication and Microstructural Examination of Reaction-Sintered Si_3N_4; a method of Microstructural Design. M. S. Thesis, Brown University, R. I. June 1975.

[58] Danforth, S. C., Richman, M. H.: Variations in Pore Structure of Reaction-Bonded Silicon Nitride (RBSN). J. Mat. Sci. 14 (1979), p. 240-241.

[59] Griffith, A. A.: The phenomena of Rupture and Flow in Solids. Phil. Trans. Roy. Soc. A221 (1920), p. 163-198.

[60] Spriggs, R. M.: Effect of Open and Closed Pores on Elastic Moduli of Polycrystalline Alumina. J. Amer. Ceram. Soc. 45 (1962), p. 454.

[61] Duckworth, W. J.: Discussion of Ryshkewitch's Paper by Winston Duckworth. J. Amer. Ceram. Soc. 36 (1953), p. 68.

[62] Bal'shin, M. Y.: Doklady Akad. Sci. USSR 67 (1949), p. 831-834.

[63] Hasselman, D.P.H.: Relation Between Effects of Porosity on Strength and on Young's Modulus of Elasticity of Polycrystalline Materials. J. Amer. Ceram. Soc. 46 (1963), p. 564-565.

[64] Passmore, E. M., Spriggs, R. M., Vasilos, T.: Strength-Grain Size-Porosity Relations in Alumina. J. Amer. Ceram. Soc. 48 (1965), p. 1-7.

[65] Rice, R. W.: Comment on Additional Observations on the Strength/Nitrided Density Relationship for a Reaction-Sintered Silicon Nitride. J. Mat. Sci. 12 (1977), p. 627-630.

[66] Jones, B. F., Pitman, K. C., Lindley, M. W.: The Development of Strength in Reaction-Sintered Silicon Nitride. J. Mat. Sci. 12 (1977), p. 563-576.

[67] Jones, B. F., Lindley, M.W.: Reply to "Comments on 'additional observations on the strength/nitrided density relationship for a reaction-sintered silicon nitride'". J. Mat. Sci. 12 (1977), p. 630-631.

[68] Dalgleish, B. J., Pratt, P. L.: The Influence of Microstructure on the Strength of Reaction-Bonded Silicon Nitride. Proc. Brit. Ceram. Soc. 25 (1975), p. 295-310.

[69] Jennings, H. M., Dalgleish, B. J., Pratt, P. L.: Relationship of Microstructure and Temperature to Fracture Mechanics Parameters in Reaction-Bonded Silicon Nitride. Ber. Dt. Keram. Ges. 55 (1978), p. 394-397.

[70] Moulson, A. J., Longland, P.: The Development of the Mechanical Strength of Reaction-Bonded Silicon Nitride. Dept. of Ceramics, Houldsworth School of Applied Science, Univ. of Leeds. Final Report, U. S. Army Research and Development Group, Agreement No. DAERo-75-G-78, Control No. 531-12943, April 1978.

[71] Mangels, J. A.: Effect of H_2-N_2 nitriding Atmosphere on the Properties of Reaction-Sintered Si_3N_4. J. Amer. Ceram. Soc. 58 (1975), p. 354-355.

[72] Danforth, S. C., Jennings, H. M., Richman, M. H.: Strength vs. Nitrided Density and Microstructural Design of Reaction-Bonded Silicon Nitride. J. Mat. Sci. 13 (1978) p. 1590-1592.

[73] Elias, D. P., Jones, B. F., Lindley, M. W.: The Formation of the α- and β-phases in reaction-sintered silicon nitride and their Influence on Strength. Powd. Met. Intern. 8 (1976), p. 162-165.

[74] Jennings, H. M., Danforth, S. C., Richman, M. H.: Strength and Microstructural Design of Silicon Nitride. Proceedings of the 2nd International Conference on Mechanical Behavior of Materials, Boston (1976) p. 1877-1881.

[75] Mangels, J. A., Cassidy, D. J.: Physical Properties of Injection-molded Silicon Nitride. Jahrestagung der Amer. Ceram. Soc., Cincinnati, 1973.

[76] Engel, W., Thuemmler, F.: Creep Behavior of Reactor-Sintered Si_3N_4 at 1200-1400°C. Ber. Dt. Keram. Ges. 50 (1973), p. 204-210.

[77] Din, S. U., Nicholson, P. S.: Creep Deformation of Reaction-Sintered Silicon Nitrides. J. Amer. Ceram. Soc. 58 (1975), p. 500-502.

[78] Birch, J. M., Wilshire, B., Owens, D. J. R., Shantaram, D.: The Influence of Stress Distribution on the Deformation and Fracture Behavior of Ceramic Materials under Compression Creep Conditions. J. Mat. Sci. 11 (1976), p. 1817-1825.

[79] Birch, J. M., Wilshire, B.: The Compression Creep Behavior of Silicon Nitride Ceramics. J. Mat. Sci. 13 (1978) p. 2627-2636.

[80] Grathwohl, G.: Creep of Reaction-Sintered Silicon Nitride. Dissertation, Kernforschungszentrum Karlsruhe, Institut fuer Material- und Festkoerperforschung, August 1978.

[81] Glenny, E., Taylor, T. A.: Mechanical Strength and Thermal-Fatigue Characteristics of Silicon Nitride. Powd. Met. 8 (1961), p. 164-195.

[82] Grathwohl, G., Thuemmler, F.: Creep of Si_3N_4 under Oxidizing and Nonoxidizing Conditions. Ber. Dt. Keram. Ges. 52 (1975), p 268-270.

[83] Grathwohl, G., Porz, F., Thuemmler, F.: On the Development of Creep-Resistant Reaction-Sintered Silicon Nitride. Ber. Dt. Keram. Ges. 53 (1976), p. 346-348.

[84] Grathwohl, G., Thuemmler, F.: Creep of Reaction-Bonded Silicon Nitride. J. Mat. Sci. 13 (1978), p. 1177-1186.

[85] Shaffer, P. T. B., Hasselman, D. P. H., Chaberski, A. Z.: Factors Affecting Thermal Shock Resistance of Polyphase Ceramic Bodies. Technical Report 60-749, Part I. New York: The Carborundum Co., 1961.

[86] Hasselman, D. P. H.: Thermal Stress Resistance Parameters for Brittle Refractory Ceramics: A Compendium. Amer. Ceram. Soc. Bull. 49 (1970), p. 1033-1037.

[87] Hasselman, D. P. H.: Unified Theory of Thermal Shock Fracture Initiation and Crack Propagation in Brittle Ceramics. J. Amer. Ceram. Soc. 52 (1969), p. 600-604.

[88] Coble, R. L., Kingery, W. D.: Effect of Porosity on Thermal Stress Fracture. J. Amer. Ceram. Soc. 38 (1955), p. 33-37.

[89] Feld, H., Fickel, A.: Contribution to the Characterization of Thermal Shock Resistance of Brittle Materials. Powd. Met. Intern. 7 (1975), p. 168-169.

[90] Claussen, N., Lahmann, C. P.: Fracture Behavior of some Hot-Pressed Si_3N_4 Ceramics at High Temperatures. Powd. Met. Intern. 7 (1975), p. 133-135.

[91] Weaver, G. Q., Baumgartner, H. R., Torti, M. L.: Thermal Shock Behavior of Sintered Silicon Carbide and Reaction-Bonded Silicon Nitride. Special Ceramics 6 (1975) p. 261-281.

[92] Anzai, K., Hashimoto, H.: Thermal Shock Resistance of Silicon Nitride. J. Mat. Sci. 12 (1977), p. 2351-2353.

[93] Glenny, E., Taylor, T. A.: Mechanical Strength and Thermal Fatigue Characteristics of Silicon Nitride. Powd. Met. 8 (1961), p. 164-195.

[94] Ziegler, G.: Thermal Shock Investigations on Silicon Nitride. Ber. Dt. Keram. Ges. 55 (1978), p. 105-109.

[95] Ryklis, E. A., Bolgar, A. S., Fesenko, V. V.: Evaporation and Thermodynamic Properties of Silicon Nitride. Soviet. Powd. Met. (Engl. Translation) (1969), p. 73-76.

[96] Handbook of Chemistry and Physics, 54th Edition, CRC Press (1973-1974)

[97] Gugel, E.: (Nichtoxidkeramik) Non-Oxide Ceramics. Handbook of Ceramics, Group II E2, copyright by Freiburg i.Br.: Schmid GmbH, 1975.

[98] Prochazka, S., Greskovich, C. D.: Development of a Sintered Process for High-Performance Silicon Nitride. AMMRC TR 78-32 (1978).

[99] Knoch, H., Ziegler, G.: Effect of Powder Composition and Sintering Temperature on Kinetics of Conversion, Structure and Mechanical Properties of Hot-Pressed Silicon Nitride. Ber. Dt. Keram. Ges. 55 (1978), p. 242-245.

[100] Beck, H.: Injection Molding, 2nd Edition. Munich: Carl Hanser Verlag, 1963.

[101] Discourse on Plastics Processing. 1. Injection molding. 2nd Edition. Ludwigshafen: BASF, 1970.

[102] Injection Molding on Thermoplastics. Frankfurt (Main): Hoechst, 1971.

[103] Thompson, J. I.: Forming Thin Ceramics. Amer. Ceram. Soc. Bull. 42 (1963), p. 480-481.

[104] Strivens, M. A.: Injection Molding of Ceramic Insulating Materials. Amer. Ceram. Soc. Bull. 42 (1963), p. 13-19.

[105] Hennicke, H. W., Neuenfeld, K.: Injection Molding Technique as a Shaping Method in Ceramics.Ber. Dt. Keram. Ges. 45 (1968), p. 469-473.

[106] Matkin, D. J., Denton, J. E., Valentine, T. M., Warrington, P.: The Fabrication of Silicon Nitride by Ceramic-Plastic Technology. Proc. Brit. Ceram. Soc. 22 (1973), p. 291-304.

[107] Wedemeyer, R.: Injection Molding of Nonplastic Ceramic Materials. Sprechsaal 109 (1976), p. 347-351.

[108] Sleptsov, V. M., Shcherbina, O. D., Trunov, G. V.: Removal of Binder from Silicon Nitride Specimens. Soviet. Powd. Met. (Engl. Translation) 14 (1975), p. 596-598.

[109] Ondracek, G.: On the Quantitative Description of the Stereometric Structure of Multiphase Materials. Science of Ceramics 6 (1973), p. III 3-III 44.

[110] Knoch, H., Leucht, R., Ziegler, G.: Methods of Studying the Structural Characteristics of Hot-Pressed Silicon Nitride. Sonderbaende der Praktischen Metallographie 9 (1978), p. 255-264.

[111] Ritter, H. L., Drake, L. C.: Pore-size Distribution in Porous Materials. Ind. Eng. Chem. Anal. Ed. 17 (1945), p. 782-786.

[112] Ilschner, B. : (Hochtemperaturplastizitaet, Warmfestigkeit und Warmverformbarkeit metallischer und nichtmetallischer Werkstoffe) High Temperature Plasticity, Hot Strength and Heat Deformability of Metallic and Nonmetallic Materials. Berlin, Heidelberg, New York: Springer Verlag, 1973.

[113] Huette: The Engineer's Pocket Book. 28. Aufl., p. 875. Berlin: Wilhelm Ernst & Son, 1955.

[114] Lin, S. S.: Comparative Studies of Metal Additives on the Nitridation of Silicon. J. Amer. Ceram. Soc. 60 (1977), p. 78-81.

[115] Dawson, W. M., Moulson, A. J.: The Combined Effects of Fe and H_2 on the Kinetics of Silicon Nitridation. J. Mat. Sci. 13 (1978), p. 2289-2290.

[116] Brucklacher, D., Dienst, W.: Creep Behavior of Ceramic Nuclear Fuels under Neutron Irradiation. J. Nucl. Mater. 42 (1972), p. 285-296.

[117] Evans, A. G., Tappin, G.: Effects of Microstructure on the Stress to Propagate Inherent Flaws. Proc. Brit. Ceram. Soc. 20 (1972), p. 275-297.

[118] Heinrich, J., Munz, D.: Strength and Fracture Toughness of Reaction Bonded Silicon Nitride with Artificial Pores. Demnaechst.

[119] Riley, F. L.: Nitridation and Reaction Bonding. Proceedings "Nitrogen Ceramics", ed. F. L. Riley, Nato Advanced Study Institutes Applied Science Series No. 23, Noordhoff International Publ. BV, (1977), p. 265-288.

[120] Amato, I., Martorana, D., Rossi, M.: The Nitriding of Silicon Powder Compacts. Powd. Met. 18 (1975), p. 339-348.

[121] Lindley, M. W., Elias, D. P., Jones, B. F., Pitman, K. C.: The Influence of Hydrogen in the Nitriding Gas on the Strength, Structure and Composition of Reaction Sintered Silicon Nitride. J. Mat. Sci. 14 (1979), p. 70-85.

[122] Dervisbegovic, H.: Department of Ceramics, Houldsworth School of Applied Science, University of Leeds, persoenliche Mitteilung.

[123] Jones, B. F., Lindley, M. W.: The Influence of Hydrogen in the Nitriding Gas on the Strength of Reaction Sintered Si_3N_4. J. Mat. Sci. 11 (1976), p. 1969-1971.

[124] Gugel, E., Hauck, N., Floerke, O. W.: Course of Reaction in the Nitriding of Silicon. Ber. Dt. Keram. Ges. 56 (1979), p. 10-14.

[125] Newman, J. C.: Fracture Analysis of Surface- and through-cracked Sheets and Plates. Engng. Fract. Mech. 5 (1973), p. 667-689.

[126] Singh, J. P., Thomas, J. R., Hasselman, D. P. H.: J. Amer. Ceram. Soc., in review.

[127] Ziegler, G., Heinrich, J. Effect of Porosity on the Thermal Shock Behavior of Reaction-Sintered Silicon Nitride. Proceedings of the 4th International Meeting on Modern Ceramics Technologies, accepted for publication.